Review

Not peer-reviewed version

# Organic Self-Assembled Monolayers as Hole Transport Layer in Inverted Perovskite Solar Cells

Yajie Fu , Chunguang Li , Yang Li *

Posted Date: 6 May 2025

doi: 10.20944/preprints202505.0128.v1

Keywords: Perovskite solar cells; Self-assembled monolayers; Hole transport layers; Anchoring groups

Preprints.org (www.preprints.org) | NOT PEER-REVIEWED | Posted: 6 May 2025 doi:10.20944/preprints202505.0128.v1

*Review*

# Organic Self-Assembled Monolayers as Hole Transport Layer in Inverted Perovskite Solar Cells

**Yajie Fu [1], Chunguang Li [1] and Yang Li [2],***

[1] Qinghai Provincial Key Laboratory of Salt Lake Materials Chemical Engineering, School of Chemical Engineering, Qinghai University, Xining 810016, China
[2] School of Energy and Materials, Shihezi University, No. 280 Beisi Road, Shihezi City, Xinjiang Uygur Autonomous Region, 832000, China
* Correspondence: yang2022@shzu.edu.cn

**Abstract:** Perovskite solar cells (PSCs) are considered as one of the most promising new generation solar cells with a low-cost manufacturing process and impressive power conversion efficiency (PCE). In particular, inverted PSCs show good prospects for commercialization due to their relatively mild preparation conditions, simple process, and easy preparation into flexible large-area devices. In recent years, self-assembled monolayers (SAMs) have been widely applied as superior hole transport layers (HTLs) for state-of-the-art inverted PSCs to enhance the device performance. This review introduces the recent studies on SAM-based hole transport layers (SAM-HTLs), summarize and comment on their properties, and discuss the relationship between molecular structure and performance parameters of devices. The classification and analysis are conducted according to both the types of anchoring groups and the number of anchoring groups in SAMs. Finally, based on the current research, the future design of new efficient SAMs is prospected.

**Keywords:** perovskite solar cells; self-assembled monolayers; hole transport layers; anchoring groups

## 1. Introduction

With the rapid development of technology and economy, the global level of intelligent mechanization has increased, leading to a continuous rise in energy demand. As fossil fuel resources become increasingly depleted and the associated global environmental crisis intensifies, solar photovoltaic (PV) power generation has emerged as one of the most sustainable renewable energy solutions due to its zero-carbon emission characteristics [1,2]. However, the current high manufacturing costs of solar cells and the need to improve photoelectric conversion efficiency (PCE) continue to constrain the development of solar PV technology[3]. To address the dual demands of enhancing energy conversion efficiency in photovoltaic devices and reducing industrial costs, research on thin-film photovoltaic technologies based on novel semiconductor materials has deepened. Current major research directions include dye-sensitized solar cells (DSCs), organic solar cells (OSCs), and organic-inorganic hybrid lead halide perovskite solar cells (PSCs). Among these, PSCs based on perovskite semiconductors have demonstrated particularly outstanding performance. This is attributed to the unique advantages of organic-inorganic hybrid perovskite materials, including their high light absorption coefficient, long carrier diffusion lengths [4], low exciton dissociation barriers [5], and tunable direct bandgap properties, while also exhibiting high defect tolerance [6].

Since their debut in 2009, the PCE of PSCs has skyrocketed from an initial 3.8% to a certified 27%, setting a new record for emerging solar cell technologies in just over a decade [7–9]. This groundbreaking progress is closely tied to their unique device architecture: as illustrated in Figure 1, high-efficiency PSCs typically adopt a sandwich configuration, with the perovskite light-absorbing layer as the core, flanked by an electron transport layer (ETL) and a hole transport layer (HTL) on either side [10–13]. In the current mainstream n-i-p (conventional, Figure 1a) and p-i-n (inverted, Figure 1b) structures, the HTL not only plays a critical role in facilitating hole extraction/migration and suppressing interfacial carrier recombination but also significantly influences the optoelectronic performance and long-term stability of devices through band alignment optimization. Key factors include the matching of HOMO/LUMO energy levels with those of the electrodes and perovskite layer [14–17]. As well as interface engineering strategies, such as surface wettability modulation of the HTL in inverted architectures [18,19]. Additionally, PSCs can be fabricated via low-temperature solution-processing methods, offering advantages like low production energy consumption and simplified manufacturing workflows, which highlight their substantial potential for industrial-scale applications [20].

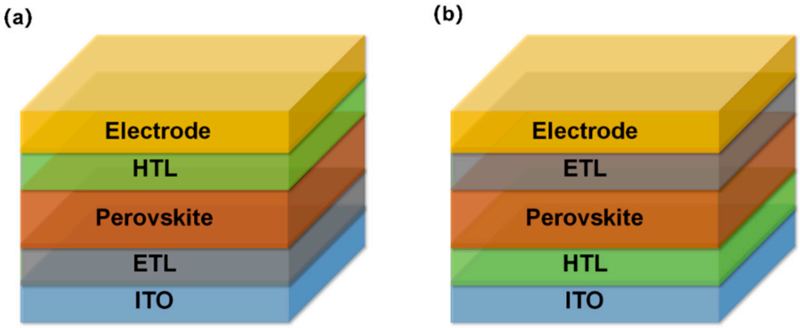

**Figure 1.** Two typical architectures of PSCs: (a) planar heterojunction conventional architecture; (b) planar heterojunction inverted architecture.

In the conventional structure of PSCs, the most classic and efficient hole transport material (HTM) is 2,2′,7,7′-tetra[N,N-di(4-methoxyphenyl)amino]-9,9′-spirobifluorene (spiro-OMeTAD). Its unique spiro-conjugated molecular core with orthogonal conformation facilitates good contact with perovskite films, while its high glass transition temperature and uniform charge transport properties enable it to maintain the highest PCE in conventional PSCs for extended periods. However, the low hole mobility caused by the stacking arrangement of its spiro-conjugated molecules necessitates performance enhancement through additives like Li-TFSI and TBP, which limits device stability [21–24]. Additionally, the high cost of spiro-OMeTAD and the requirement for a thick deposition layer (>100 nm) to achieve high efficiency significantly hinder its commercial viability [25].In contrast, inverted PSCs demonstrate stronger industrialization potential due to their compatibility with flexible substrates, applicability in perovskite-silicon tandem devices, support for dopant-free HTL, and compatibility with low-cost metal electrodes [26]. Recent advances in perovskite crystallization optimization and novel HTL development have enabled inverted devices to surpass the performance of conventional structures. Early inverted HTLs primarily used materials like poly[bis(4-phenyl)(2,4,6-trimethylphenyl) amine] (PTAA) and PEDOT: PSS [27,28], but these suffer from issues such as low mobility, high cost, and high material consumption. In this context, self-assembled monolayers (SAMs) technology has emerged as a breakthrough due to their molecular-level thickness (<1 nm), ultra-low material consumption, compatibility with green solvent processing, and exceptional interface passivation capabilities [29–31]. SAMs not only circumvent the hole mobility limitations of traditional thick films but also enable precise energy-level alignment through tailored molecular design, significantly enhancing the performance of single-junction PSCs. Moreover, SAMs exhibit unique advantages in multi-junction devices such as perovskite-perovskite and perovskite-silicon tandems: their ultrathin nature minimizes parasitic absorption, and their flexible film-forming capability adapts well to textured substrate surfaces, offering new pathways for large-scale manufacturing [32,33].

## 2. Self-Assembled Monolayers

The formation of SAMs involves selective anchoring of organic molecules onto substrate surfaces through characteristic functional groups, constructing ordered films with a precisely controlled thickness down to a single molecular layer. The self-ass represents a thermically driven spontaneous, on intermolecular to achieve self-alignment. Typically, within SAMs vertically relative to the, often exhibiting a characteristic tilt angle with respect to the surface normal. By strategically modulating the configuration of molecular backbones, intermolecular interactions can be effectively optimized, thereby enabling precise regulation of layer packing orientation [34].

### *2.1. Structural Composition and Anchoring Mechanisms of SAMs*

As illustrated in Figure 2a, in PSCs, SAMs serving as the core molecular design for HTLs typically comprise three key structural units: terminal group, linker unit and anchor group. Their overall architecture shares a high resemblance to small-molecule dyes in DSCs, with some systems even directly adopting DSC-derived dye molecules [35]. These three structural units synergistically regulate interfacial physicochemical properties, directly determining device performance. Anchor group: Through specific chemical moieties (e.g., phosphonic acid, carboxylic acid), stable interfacial binding with the metal oxide substrate is achieved, governing the molecular surface coverage density, orientation, and interfacial dipole distribution. The interaction mode between anchoring groups and substrates (e.g., coordination bonds or hydrogen bonds) critically impacts the magnitude of substrate work function adjustment, contact resistance, and carrier recombination behavior. Variations in binding strength and stability among anchoring groups further influence long-term operational reliability. Linker unit: Serving as the molecular backbone to connect anchoring and terminal groups, its chemical structure (e.g., aliphatic chains or conjugated aromatic rings) dictates the spatial arrangement of the monolayer. Non-conjugated linker units form densely ordered molecular layers through weak intermolecular interactions, acting as physical barriers or tunneling layers for carrier transport. In contrast, conjugated linker units establish lateral charge transport pathways via molecular orbital overlap, significantly enhancing film conductivity. The electronic structure of linkers also affects charge transport decay, with conjugated systems typically exhibiting superior charge retention capabilities. Terminal group: As the direct contact interface with the perovskite active layer, its electronic characteristics and chemical activity determine interfacial energy level alignment and charge extraction efficiency. By designing electron-rich heterocyclic systems (e.g., carbazole, phenothiazine derivatives), terminal groups can form chemical coordination with the perovskite surface while fine-tuning the band bending direction. This interaction not only reduces interfacial defect density but also induces an energy-level gradient favorable for hole transport, thereby suppressing charge recombination and enhancing carrier collection efficiency.

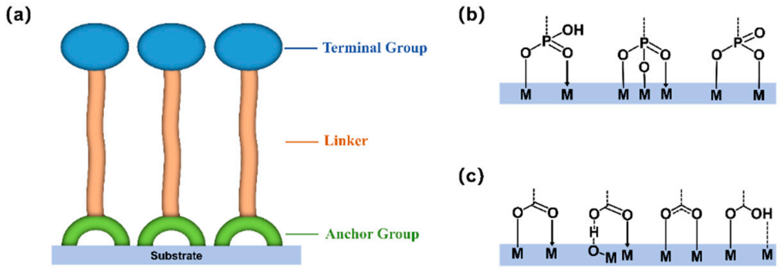

**Figure 2.** (a) Chemical structures of SAMs; Schematic diagram of the anchoring mechanism of (b) phosphonic acid and (c) carboxylic acid on substrates.

In SAMs research, carboxylic and phosphonic acid anchoring groups have garnered significant attention due to their diverse binding modes with conductive substrates (e.g., ITO, FTO) or metal oxide charge transport layers (NiO$_x$, SnO$_2$, Al$_2$O$_3$, etc.). As illustrated in Figure 2b, phosphonic acid groups, leveraging the synergy of two hydroxyls and a phosphoryl group, enable mono-, bi-, or even tridentate binding. Tridentate binding involves hydrogen transfer to form oxygen vacancies, thereby establishing a third bond. Carboxylic acid groups utilize dual binding sites—hydroxyl and carbonyl groups—to form mono- or bidentate bonding with metal oxide surfaces: monodentate bonding involves the condensation of anchoring -OH with surface hydroxyls to generate C-O-M bonds, while bidentate bonding is triggered by hydrogen transfer-induced secondary condensation [36]. Chemical interactions such as chelation, bridging coordination, and hydrogen bonding directly govern the interfacial stability between SAMs and substrates.

Current research predominantly employs ITO, FTO, and their composite substrates with $NiO_x$ as carriers for SAMs. ITO dominates due to its high transparency, excellent conductivity, and surface flatness [37]. However, its smooth surface leads to significant optical losses in inverted PSCs. To address this, Edward H. Sargent's team introduced FTO substrates [38], where the textured surface morphology reduces reflection losses and prolongs the light path, markedly enhancing the short-circuit current density ($J_{SC}$). Nevertheless, the rough surfaces of FTO result in non-uniform SAM coverage, an issue also observed in ITO-based systems. Recent studies reveal that incorporating a $NiO_x$ interlayer effectively promotes heterocondensation and optimizes SAMs' morphological uniformity. For instance, Liu's team [39] utilized an ITO/$NiO_x$/2PACz structure to prevent direct contact between perovskite and ITO. DFT calculations confirmed higher binding energy between 2PACz and $NiO_x$, along with interface defect passivation. Mariadriana Creatore's team [40] constructed an ITO/$NiO_x$/MeO-2PACz architecture, demonstrating that $NiO_x$ surfaces facilitate more uniform SAM growth. Additionally, You's team [41] employed $H_2O_2$ modification to modulate $NiO_x$ dispersion, suppress particle agglomeration, and elevate $Ni^{3+}$ content to form a highly conductive NiOOH phase. Coupled with an FTO/$NiO_x$/Me-4PACz configuration, this approach achieved a certified efficiency of 25.5% (25.2%).

## *2.2. Deposition Methods of SAMs*

In PSCs, fabrication methods for SAMs include chemical bath deposition (CBD) (dipping method), spin-coating, perovskite co-deposition, and vacuum evaporation [42–45]. Chemical bath deposition involves immersing the substrate in a SAM solution to allow molecular self-assembly and adsorption onto the surface. Precise control over adsorption density can be achieved by adjusting solvent type, solution concentration, and immersion time. This method is particularly suited for large-area or textured substrates. Subsequent annealing strengthens molecular-substrate binding, followed by solvent rinsing to remove unanchored molecules and clusters, thereby ensuring the formation of a dense monolayer fil [46,47]. Spin-coating, on the other hand, employs a spin coater to rapidly spread SAM precursor solutions across the substrate. Post-annealing enhances interfacial binding, and residual molecules are rinsed away [48]. Due to its operational simplicity and high-throughput film formation, spin-coating has become the preferred method for laboratory-scale studies.

Recent studies have advanced co-deposition techniques for SAMs and perovskite, where self-assembling molecules are directly blended into the perovskite precursor solution [49]. During spin-coating and subsequent annealing, SAMs molecules spontaneously migrate and accumulate at the substrate interface, simultaneously forming both the perovskite active layer and the bottom SAMs modification layer. This approach significantly simplifies the complexity of traditional stepwise processes while enabling synergistic optimization of interface passivation and energy-level alignment. For example: Luther's team achieved a high efficiency of 24.5% using the Me-4PACz co-deposition process [49] . Li's team realized a certified efficiency of 26.7% through in situ self-assembly of LS2 molecules [50] . However, only a limited number of specific molecules currently demonstrate superior performance with this method, and its general applicability requires further exploration. Additionally, vacuum evaporation via physical vapor deposition (PVD) enables the formation of conformal and uniform SAMs layers on rough substrates, offering advantages in reproducibility and scalability. For instance, Jen's team reported a certified efficiency of 23.50% using thermally evaporated CbzNaphPPA [51] . Despite its potential, this method demands specialized equipment and remains less utilized in current research [45].

doi:10.20944/preprints202505.0128.v1

In summary, chemical bath deposition and spin-coating, as mainstream techniques, have reached a relatively mature stage. Co-deposition technology exhibits industrialization potential due to its simplified workflow, while vacuum evaporation offers novel strategies for specialized substrate processing. Moving forward, further optimization of co-deposition molecular design and the development of low-temperature, high-efficiency evaporation processes are imperative to advance the application of SAMs in the scalable manufacturing of PSCs.

## 3. Role of SAMs in PSCs

In inverted PSCs, p-type SAMs optimize device performance through multi-level interfacial engineering. Their mechanisms of action revolve around interface modulation, charge transport, and stability enhancement, demonstrating unique advantages distinct from traditional hole transport materials. The four main roles of SAM in PSCs are as follows (Figure 3): (1) Interfacial Dipole and Energy Level Alignment. Molecular design of p-type SAMs enables flexible energy level tuning. Through dipole effects from terminal functional groups, SAMs create work function gradients between the hole transport layer and perovskite active layer, bridging their energy level mismatches. For instance, SAMs with electron-rich groups induce dipole fields pointing toward the perovskite layer at the interface, significantly reducing hole extraction energy barriers and laying the foundation for efficient photogenerated carrier separation [52]. (2) Perovskite Crystallization and Defect Passivation. During perovskite film formation, molecular frameworks of p-type SAMs directionally couple with perovskite precursors via non-covalent interactions (e.g., π-π stacking, hydrogen bonding), guiding grain growth along specific orientations [53]. This molecular-scale templating effect suppresses random nucleation, promoting the formation of dense, large-grain perovskite films. Simultaneously, anchoring groups in SAMs bond with uncoordinated metal ions on the substrate surface, reducing interfacial dangling bonds and thereby lowering non-radiative recombination channel density [54]. (3) Hole Transport Pathway Optimization: The conjugated backbone structures of p-type SAMs provide continuous molecular orbital channels for carrier transport. Their ultrathin nature not only shortens hole tunneling distances but also enhances lateral charge mobility through intermolecular π-electron delocalization, enabling efficient and selective hole transport [55]. Compared to traditional polymeric hole transport materials, the low thickness of SAMs avoids carrier scattering losses caused by bulk defect accumulation. (4) Interfacial Stability Enhancement: Chemical modifications of p-type SAMs can introduce hydrophobic groups (e.g., fluorinated groups), constructing dynamic barriers at the perovskite/electrode interface. These barriers simultaneously block environmental moisture/oxygen penetration and suppress halide ion migration within the perovskite layer, thereby delaying interfacial delamination and chemical degradation [56,57].

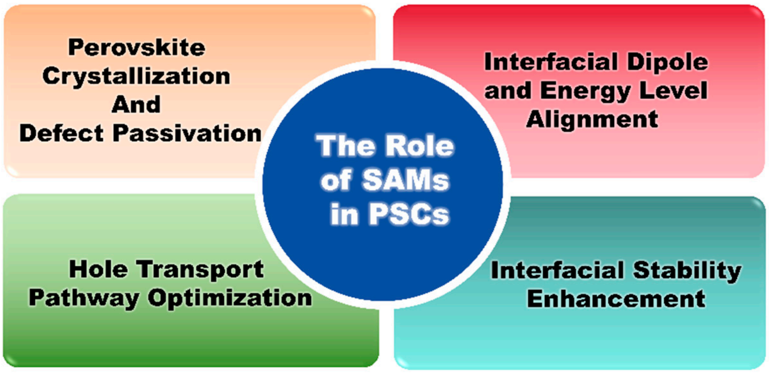

**Figure 3.** The function of SAMs in PSCs.

## 4. Application of SAMs in Perovskite Solar Cells

In 2018, Vytautas Getautis and colleagues proposed that the phosphoric acid structure in HTL molecules can be anchored by transparent conductive oxides to form ultra-thin SAMs [58]. SAM-based PSCs demonstrated performance comparable to those using traditional organic HTMs. Recent studies have shown that SAMs, when employed as HTLs in p-i-n structured PSCs, effectively passivate interface defects, thereby enhancing the stability and performance of PSCs while facilitating hole extraction [59–62]. Compared to HTMs, SAMs offer advantages such as a simpler fabrication process, strong molecular structural flexibility, low parasitic absorption, and reduced material consumption[63,64]. In recent years, the rapid development of p-type PSCs has greatly benefited from the application of SAMs.

This review summarizes the latest research progress on SAMs-based hole transport layer (SAMs-HTLs), and discuss the relationship between molecular structure and performance parameters of devices in detail. The chemical structures of SAMS are shown in Figures 4, 8, 10, and 13, with the corresponding photovoltaic parameters summarized in Tables 1–3. The classification and analysis are conducted according to both the types of anchoring groups and the number of anchoring groups in SAMs, distinguishing this work from previous reviews that primarily focused on functional group classifications [65]. Finally, based on the current research, the future design of new efficient SAMs is prospected.

**Table 1.** The energy level of SAMs with phosphonic acid as the anchor group and their performance parameters in the PSCs.

| SAMs | HOMO（eV） | Device structure | $V_{OC}$ (V) | $J_{SC}$ (mA/cm$^2$) | FF(%) | PCE(%) | Ref. |
|---|---|---|---|---|---|---|---|
| **V1036** | -4.7 | ITO/V1036+C4/$Cs_{0.05}(MA_{0.17}FA_{0.83})_{0.95}Pb(I_{0.83}Br_{0.17})_3$/$C_{60}$/BCP/Cu | 1.09 | 21.4 | 76.5 | 17.8 | [58] |
| **MeO-2PACz** | -5.1 | ITO/MeO-2PACz/$Cs_{0.05}(MA_{0.17}FA_{0.83})_{0.95}Pb(I_{0.83}Br_{0.17})_3$/$C_{60}$/BCP/Cu (Ag) | 1.144 | 21.9 | 80.2 | 20.8 | [66] |
| **DC-PA** | -5.38 | ITO/DC-PA+IAHA/$Cs_{0.05}MA_{0.15}FA_{0.80}PbI_3$/PI/$C_{60}$/BCP/Ag | 1.16 | 24.66 | 82.45 | 23.59 | [67] |
| **BrNH3-4PACz** | -5.18 | ITO/BrNH3-4PACz/$Cs_{0.05}FA_{0.70}MA_{0.25}Sn_{0.5}Pb_{0.5}I_3$/EDA/$C_{60}$/BCP/Ag | 0.88 | 32 | 82 | 23 | [68] |
| **2PACz** | -5.44 | ITO/ 2PACz / $Cs_{0.2}FA_{0.8}PbI_3$/$C_{60}$/BCP/Ag | 1.01 | 21.87 | 79.23 | 17.5 | [70] |
| **C-2PACz** | -5.46 | ITO/ C-2PACz / $Cs_{0.2}FA_{0.8}PbI_3$/$C_{60}$/BCP/Ag | 1.05 | 22.45 | 77.37 | 18.16 | [70] |
| **S-2PACz** | -5.48 | ITO/ S-2PACz / $Cs_{0.2}FA_{0.8}PbI_3$/$C_{60}$/BCP/Ag | 1.05 | 22.66 | 78.65 | 18.65 | [70] |
| **o-PhPACz** | -5.00 | FTO/ o-PhPACz / perovskite/$C_{60}$/BCP/Ag | 1.16 | 25.81 | 83.5 | 24.7 | [71] |
| **m-PhPACz** | -5.01 | FTO/ m-PhPACz / perovskite/$C_{60}$/BCP/Ag | 1.18 | 25.8 | 85.4 | 26.2 | [71] |
| **p-PhPACz** | -5.22 | FTO/ p-PhPACz / perovskite/$C_{60}$/BCP/Ag | 1.17 | 25.78 | 82 | 25.5 | [71] |
| **SAB** | -5.57 | FTO/ SAB / $FA_{0.84}MA_{0.11}Cs_{0.05}$ $Pb(I_{0.987}Br_{0.013})_3$/$C_{60}$/BCP/Ag | 1.174 | 26.2 | 85.5 | 26.3 | [72] |
| **Br-2EPT** | -5.47 | TCO/Br-2EPT/$FA_{0.92}MA_{0.08}Pb(I_{0.92}Br_{0.08})_3$/$C_{60}$/BCP/Cu | 1.09 | 25.11 | 82 | 22.44 | [55] |
| **2BrPTZAP** | -5.77 | ITO/2BrPTZAP/$Cs_{0.05}(FA_{0.85}MA_{0.15})_{0.95}Pb(I_{0.85}Br_{0.15})_3$/PCBM/BCP/Ag | 1.18 | 22.29 | 80.02 | 22.06 | [73] |
| **2BrPXZAP** | -5.59 | ITO/2BrPXZAP/$Cs_{0.05}(FA_{0.85}MA_{0.15})_{0.95}Pb(I_{0.85}Br_{0.15})_3$/PCBM/BCP/Ag | 1.19 | 22.51 | 81.69 | 22.93 | [73] |
| **DMAcPA** | -5.98 | ITO/(DMAcPA)Perovskite/PEABr/PCBM/BCP/Ag | 1.187 | 25.69 | 84.73 | 25.86 | **[74]** |
| **MeO-BTBT** | -5.39 | ITO/MeO-BTBT/$Cs_{0.05}MA_{0.15}FA_{0.80}PbI_3$/PI/$C_{60}$/BCP/Ag | 1.16 | 24.87 | 85.28 | 24.53 | [75] |
| **CbzPh** | -5.36 | ITO/CbzPh/$Cs_{0.05}MA_{0.15}FA_{0.80}PbI_3$/PI/$C_{60}$/BCP/Ag | 1.12 | 23.43 | 73.06 | 19.2 | [76] |

| | | | | | | | |
|---|---|---|---|---|---|---|---|
| **CbzNaph** | -5.24 | ITO/CbzNaph/$Cs_{0.05}MA_{0.15}FA_{0.80}PbI_3$/PI/$C_{60}$/BCP/Ag | 1.17 | 24.69 | 83.39 | 24.1 | [76] |
| **BCB10Br-C4PA** | -5.63 | ITO/BCB10Br-C4PA/$FA_{0.8}Cs_{0.2}Pb(I_{0.6}Br_{0.4})_3$/$C_{60}$/ALD-$SnO_2$/Cu | 1.286 | 17.54 | 82.61 | 18.63 | [77] |
| | | four-terminal TSC:ITO/BCB10Br-C4PA/$FA_{0.8}Cs_{0.2}Pb(I_{0.6}Br_{0.4})_3$/$C_{60}$ /ALD-$SnO_2$/transparentelectrode/glass/ITO /PEDOT:PSS/$(FASnI_3)_{0.6}(MAPbI_3)_{0.4}$/$C_{60}$/BCP/Cu | 1.264 | / | / | 26.24 | |
| **DCB-BPA** | -5.56 | ITO/DCB-BPA/$FA_{0.8}Cs_{0.2}PbI_{1.8}Br_{1.2}$/$C_{60}$/BCP/Cu | 1.33 | 17.75 | 82.70 | 19.53 | [78] |
| | | four-terminal TSC:ITO/DCB-BPA/$FA_{0.8}Cs_{0.2}PbI_{1.8}Br_{1.2}$/$C_{60}$/$SnO_2$ /IZO/transparentelectrode/glass/ITO/PEDOT:PSS/$(FASnI_3)_{0.6}$ $(MAPbI_3)_{0.4}$/$C_{60}$/BCP/Cu | / | / | / | 26.90 | |
| **CbzBF** | -5.50 | ITO/CbzBF/$Cs_{0.05}MA_{0.15}FA_{0.80}PbI_3$/PI/$C_{60}$/BCP/Ag | 1.09 | 24.00 | 83.04 | 21.72 | [79] |
| **CbzBT** | -5.54 | ITO/CbzBT/$Cs_{0.05}MA_{0.15}FA_{0.80}PbI_3$/PI/$C_{60}$/BCP/Ag | 1.16 | 24.54 | 84.41 | 24.04 | [79] |
| **4PACz** | -5.43 | ITO/4PACz /$Cs_{0.05}(FA_{0.98}MA_{0.02})_{0.95}Pb(I_{0.98}Br_{0.02})_3$/LiF/$C_{60}$ /BCP/Ag | 1.14 | 25.2 | 78.1 | 22.4 | [80] |

**Table 1（Continued）**

| SAMs | HOMO（eV） | Device structure | $V_{OC}$ (V) | $J_{SC}$ (mA/cm$^2$) | FF(%) | PCE(%) | Ref. |
|---|---|---|---|---|---|---|---|
| **SAX** | -5.49 | ITO/SAX/$Cs_{0.05}(FA_{0.98}MA_{0.02})_{0.95}Pb(I_{0.98}Br_{0.02})_3$/LiF/$C_{60}$ /BCP/Ag | 1.17 | 25.7 | 83.4 | 25.1 | [80] |
| **MeO-PhPACz** | -5.61 | ITO/MeO-PhPACz/$Cs_{0.05}FA_{0.8}MA_{0.15}Pb(I_{0.75}Br_{0.25})_3$/$C_{60}$/BCP/Ag | 1.14 | 24.83 | 82.0 | 23.24 | [81] |
| **PPA** | -5.28 | ITO/PPA/$Cs_{0.05}FA_{0.85}MA_{0.1}PbI_3$/OABr/PCBM/BCP/Ag | 1.10 | 24.70 | 79.2 | 21.52 | [82] |
| **1PATAT-C3** | -5.46 | ITO or FTO/1PATAT-C3/$Cs_{0.05}FA_{0.80}MA_{0.15}PbI_{2.75}Br_{0.25}$/ $EDAI_2$/$C_{60}$/BCP/Ag | 1.06 | 24.00 | 82 | 21.1 | [83] |
| **2PATAT-C3** | -5.49 | ITO or FTO/2PATAT-C3/$Cs_{0.05}FA_{0.80}MA_{0.15}PbI_{2.75}Br_{0.25}$/ $EDAI_2$/$C_{60}$/BCP/Ag | 1.14 | 23.3 | 83 | 22.2 | [83] |
| **3PATAT-C3** | -5.48 | ITO or FTO/3PATAT-C3/$Cs_{0.05}FA_{0.80}MA_{0.15}PbI_{2.75}Br_{0.25}$/ $EDAI_2$/$C_{60}$/BCP/Ag | 1.13 | 24.5 | 83 | 23.0 | [83] |
| **3PATAT-C4** | -5.5 | ITO or FTO/3PATAT-C4/$Cs_{0.05}FA_{0.80}MA_{0.15}PbI_{2.75}Br_{0.25}$/ $EDAI_2$/$C_{60}$/BCP/Ag | 1.14 | 23.3 | 83 | 22.1 | [83] |
| **IDCz-1** | -4.94 | FTO/ IDCz-1/$Cs_{0.05}FA_{0.85}MA_{0.1}PbI_3$/PI/$C_{60}$/BCP/Ag | 1.01 | 25.27 | 81.92 | 20.97 | [84] |
| **IDCz-2** | -5.11 | FTO/ IDCz-2/$Cs_{0.05}FA_{0.85}MA_{0.1}PbI_3$/PI/$C_{60}$/BCP/Ag | 1.11 | 25.43 | 81.61 | 23.11 | [84] |
| **IDCz-3** | -5.26 | FTO/ IDCz-3/$Cs_{0.05}FA_{0.85}MA_{0.1}PbI_3$/PI/$C_{60}$/BCP/Ag | 1.16 | 25.59 | 84.74 | 25.15 | [84] |
| **D-3PACz** | -5.06 | ITO/$NiO_x$/D-3PACz/$FAPbI_3$/PCBM/ BCP/Ag | 1.14 | 25.29 | 82.5 | 23.8 | [85] |

**Table 2.** The energy level of SAMs with carboxylic acid as the anchor group and their performance parameters in the PSCs.

| SAMs | HOMO（eV） | Device structure | $V_{OC}$ (V) | $J_{SC}$ (mA/cm$^2$) | FF(%) | PCE(%) | Ref |
|---|---|---|---|---|---|---|---|
| **TPA** | -5.33 | ITO/TPA/$MAPbI_3$/PCBM/BCP/Ag | 1.06 | 19.4 | 77 | 15.9 | [86] |
| **MC-43** | -5.11 | ITO/MC-43/$MAPbI_3$/PCBM/BCP/Ag | 1.07 | 20.3 | 80 | 17.3 | [86] |
| **RC-24** | -5.13 | ITO/RC-24/$Cs_{0.05}FA_{0.79}MA_{0.16}Pb(I_{0.84}Br_{0.16})_3$/$C_{60}$/BCP/Cu | 1.123 | 22.3 | 79 | 19.8 | [87] |
| **RC-25** | -5.22 | ITO/RC-25/$Cs_{0.05}FA_{0.79}MA_{0.16}Pb(I_{0.84}Br_{0.16})_3$/$C_{60}$/BCP/Cu | 1.116 | 22.1 | 79 | 19.6 | [87] |
| **RC-34** | -5.32 | ITO/RC-34/$Cs_{0.05}FA_{0.79}MA_{0.16}Pb(I_{0.84}Br_{0.16})_3$/$C_{60}$/BCP/Cu | 1.109 | 22.5 | 79 | 19.7 | [87] |

| | | | | | | | |
|---|---|---|---|---|---|---|---|
| **MC-45** | -5.12 | ITO/MC-45/$Cs_{0.05}FA_{0.79}MA_{0.16}Pb(I_{0.84}Br_{0.16})_3$/$C_{60}$/BCP/Ag | 1.09 | 20.56 | 74.35 | 16.69 | [88] |
| **MC-54** | -5.16 | ITO/MC-54/$Cs_{0.05}FA_{0.79}MA_{0.16}Pb(I_{0.84}Br_{0.16})_3$/$C_{60}$/BCP/Ag | 1.10 | 22.32 | 79.15 | 19.52 | [88] |
| **MC-55** | -5.26 | ITO/MC-55/$Cs_{0.05}FA_{0.79}MA_{0.16}Pb(I_{0.84}Br_{0.16})_3$/$C_{60}$/BCP/Ag | 1.09 | 21.90 | 79.32 | 18.99 | [88] |
| **2F** | -5.42 | ITO/2F/$FA_{0.8}Cs_{0.2}Pb(I_{0.6}Br_{0.4})_3$/TEACl/$C_{60}$/SnO2/Cu<br>ITO/2F/$FA_{0.8}Cs_{0.2}Pb(I_{0.95}Br_{0.05})_3$/TEACl/$C_{60}$/$SnO_2$/Cu<br>ITO/2F/$FA_{0.6}MA_{0.3}Cs_{0.1}Pb_{0.5}Sn_{0.5}I_3$/$EDAI_2$/$C_{60}$/$SnO_2$/Cu | 1.31<br>1.15<br>0.872 | 17.93<br>23.59<br>32.55 | 82.31<br>82.42<br>81.89 | 19.33<br>22.36<br>23.24 | [89] |
| **TBT-BA** | -5.10 | ITO/TBT-BA /$Cs_{0.04}(FA_{0.96}MA_{0.04})_{0.96}Pb(I_{0.96}Br_{0.04})_3$ /PEAI/PCBM/BCP/Ag | 1.19 | 24.9 | 83.7 | 24.8 | [90] |
| **TBT-FBA** | -5.15 | ITO/TBT-FBA /$Cs_{0.04}(FA_{0.96}MA_{0.04})_{0.96}Pb(I_{0.96}Br_{0.04})_3$ /PEAI/PCBM/BCP/Ag | 1.17 | 24.8 | 82.4 | 24.0 | [90] |

**Table 2（Continued）**

| SAMs | HOMO（eV） | Device structure | $V_{OC}$ (V) | $J_{SC}$ (mA/cm$^2$) | FF(%) | PCE(%) | Ref |
|---|---|---|---|---|---|---|---|
| **TBT-DBA** | -5.21 | ITO/TBT-DBA /$Cs_{0.04}(FA_{0.96}MA_{0.04})_{0.96}Pb(I_{0.96}Br_{0.04})_3$ /PEAI/PCBM/BCP/Ag | 1.13 | 25.0 | 81.5 | 23.1 | [90] |
| **MPA-2FBT-BA** | -4.91 | ITO/ MPA-2FBT-BA /$MAPbI_3$/$PC_{61}BM$/BCP/Ag | 1.13 | 22.79 | 78.95 | 20.32 | [91] |
| **3CATAT-C3** | -5.46 | ITO/3CATAT-C3 /$Cs_{0.05}FA_{0.80}MA_{0.15}PbI_{2.75}Br_{0.25}$/$EDAI_2$/$C_{60}$/BCP/Ag | 1.11 | 25.1 | 83 | 23.1 | [92] |
| **9CPA** | -5.19 | FTO/9CPA/$Cs_{0.1}FA_{0.6}MA_{0.3}Pb_{0.5}Sn_{0.5}I_3$/$C_{60}$/BCP/Ag | 0.89 | 32.5 | 76 | 22.1 | [93] |
| **9CAA** | -5.35 | FTO/9CAA/$Cs_{0.1}FA_{0.6}MA_{0.3}Pb_{0.5}Sn_{0.5}I_3$/$C_{60}$/BCP/Ag | 0.89 | 32.8 | 79 | 23.1 | [93] |
| **NaPA** | -6.68 | ITO/ NaPA /$FA_{0.9}MA_{0.05}Cs_{0.05}PbI_3$/LiF/$C_{60}$/BCP/Ag | 0.928 | 24.5 | 69.8 | 15.9 | [94] |
| **AnPA** | -6.07 | ITO/ AnPA /$FA_{0.9}MA_{0.05}Cs_{0.05}PbI_3$/LiF/$C_{60}$/BCP/Ag | 1.017 | 24.6 | 76.5 | 19.1 | [94] |
| **Py1** | -5.92 | ITO/ Py1/$FA_{0.9}MA_{0.05}Cs_{0.05}PbI_3$/LiF/$C_{60}$/BCP/Ag | 1.095 | 25.0 | 81.3 | 22.3 | [94] |
| **Py2** | -5.56 | ITO/ Py2/$FA_{0.9}MA_{0.05}Cs_{0.05}PbI_3$/LiF/$C_{60}$/BCP/Ag | 1.151 | 26.1 | 84.1 | 25.2 | [94] |

**Table 3.** The energy level of SAMs with cyanoacetic acid as the anchor group and their performance parameters in the PSCs.

| SAMs | HOMO（eV） | Device structure | $V_{OC}$ (V) | $J_{SC}$ (mA/cm$^2$) | FF(%) | PCE(%) | Ref |
|---|---|---|---|---|---|---|---|
| **MPA-BT-CA** | -5.29 | ITO/MPA-BT-CA/$(FA_{0.17}MA_{0.94}PbI_{3.11})_{0.95}(PbCl_2)_{0.05}$/$C_{60}$/BCP/Ag | 1.13 | 22.25 | 84.8 | 21.24 | [95] |
| **FMPA-BT-CA** | -5.45 | ITO/FMPA-BT-RA/perovskite/$C_{60}$/BCP/Cu | 1.151 | 23.33 | 83.3 | 22.37 | [56] |
| **2FMPA-BT-CA** | -5.37 | ITO/2FMPA-BT-RA/perovskite/$C_{60}$/BCP/Cu | 1.143 | 22.81 | 83.1 | 21.68 | [56] |
| **Cz-CA** | -5.72 | ITO/Cz-CA/$Cs_{0.05}(MA_{0.08}FA_{0.92})_{0.95}Pb(I_{0.92}Br_{0.08})_3$/PEAI/PCBM/$C_{60}$/BCP/Ag | / | / | / | 20.17 | [96] |
| **TPA-CA** | -5.87 | ITO/TPA-CA/$Cs_{0.05}(MA_{0.08}FA_{0.92})_{0.95}Pb(I_{0.92}Br_{0.08})_3$/PEAI/PCBM/$C_{60}$/BCP/Ag | / | / | / | 20.66 | [96] |
| **MPA-CA** | -5.45 | ITO/MPA-CA/$Cs_{0.05}(MA_{0.08}FA_{0.92})_{0.95}Pb(I_{0.92}Br_{0.08})_3$/PEAI/PCBM/$C_{60}$/BCP/Ag | / | / | / | 17.58 | [96] |

| | | | | | | | |
|---|---|---|---|---|---|---|---|
| **Cz-Ph-CA** | -5.53 | ITO/Cz-Ph-CA/$Cs_{0.05}(MA_{0.08}FA_{0.92})_{0.95}Pb(I_{0.92}Br_{0.08})_3$/PEAI/PCBM/$C_{60}$/BCP/Ag | / | / | / | 20.26 | [96] |
| **TPA-Ph-CA** | -5.61 | ITO/TPA-Ph-CA/$Cs_{0.05}(MA_{0.08}FA_{0.92})_{0.95}Pb(I_{0.92}Br_{0.08})_3$/PEAI/PCBM/$C_{60}$/BCP/Ag | / | / | / | 20.36 | [96] |
| **MPA-Ph-CA** | -5.39 | ITO/MPA-Ph-CA/$Cs_{0.05}(MA_{0.08}FA_{0.92})_{0.95}Pb(I_{0.92}Br_{0.08})_3$/PEAI/PCBM/$C_{60}$/BCP/Ag | 1.139 | 23.55 | 84.02 | 22.53 | [96] |

**Table 3（Continued）**

| SAMs | HOMO（eV） | Device structure | $V_{OC}$ (V) | $J_{SC}$ (mA/cm$^2$) | FF(%) | PCE(%) | Ref |
|---|---|---|---|---|---|---|---|
| **TPAT-CA** | -5.24 | ITO/TPAT-CA/$FASnI_3$/$C_{60}$/BCP/Ag | 0.58 | 19.2 | 72.6 | 8.1 | [97] |
| **FNE29** | -5.04 | ITO/FNE29/$MAPbI_3$/PCBM/BCP/Ag | 1.038 | 22.68 | 71.2 | 16.75 | [98] |
| **DT-1** | -5.37 | ITO/DT-1/$MAPbI_3$/PCBM/BCP/Ag | 1.11 | 23.00 | 80.9 | 20.65 | [98] |

### *4.1. SAMs Anchored with Phosphonic Acid*

Phosphoric acid, as a mainstream anchoring group, has been widely utilized in SAMs for PSCs. In existing studies, its terminal groups encompass carbazole-based, triphenylamine-based, and acridine-derived moieties, while the molecular linkers typically employ alkyl chains or aromatic ring structures as bridging units. These SAMs demonstrate exceptional interfacial modulation capabilities in perovskite photovoltaic devices across varying bandgap values. As illustrated in the Figure 4, we summarize the molecular structures of phosphate-anchored SAMs, with the corresponding device performance parameters listed in the accompanying Table 1.

Getautis et al. [58] used SAM named V1036 with phosphate anchor group for HTL of p-i-n PSCs to achieve PCE equivalent to PTAA-based devices, showing for the first time the great potential of SAM for HTL application. Then, the research group [66] simplified the end group of V1036 to obtain MeO-2PACz, and both single-junction PSCs and laminated PSCs based on MeO-2PACz achieved excellent performance. The position of the methoxy substituent on MeO-2PACz also affects its properties. Alex K.-Y. Jen et al. [67] synthesized DC-PA by adjusting the position of the MeO-2PACz methoxy substituent on the carbazole unit. They combined DC-PA with 5-aminocaproate hydro iodate (IAHA) as HTL. IAHA further facilitated the interaction with the top perovskite layer. The maximum PCE of the PSC was 23.59% and the stability was also improved.

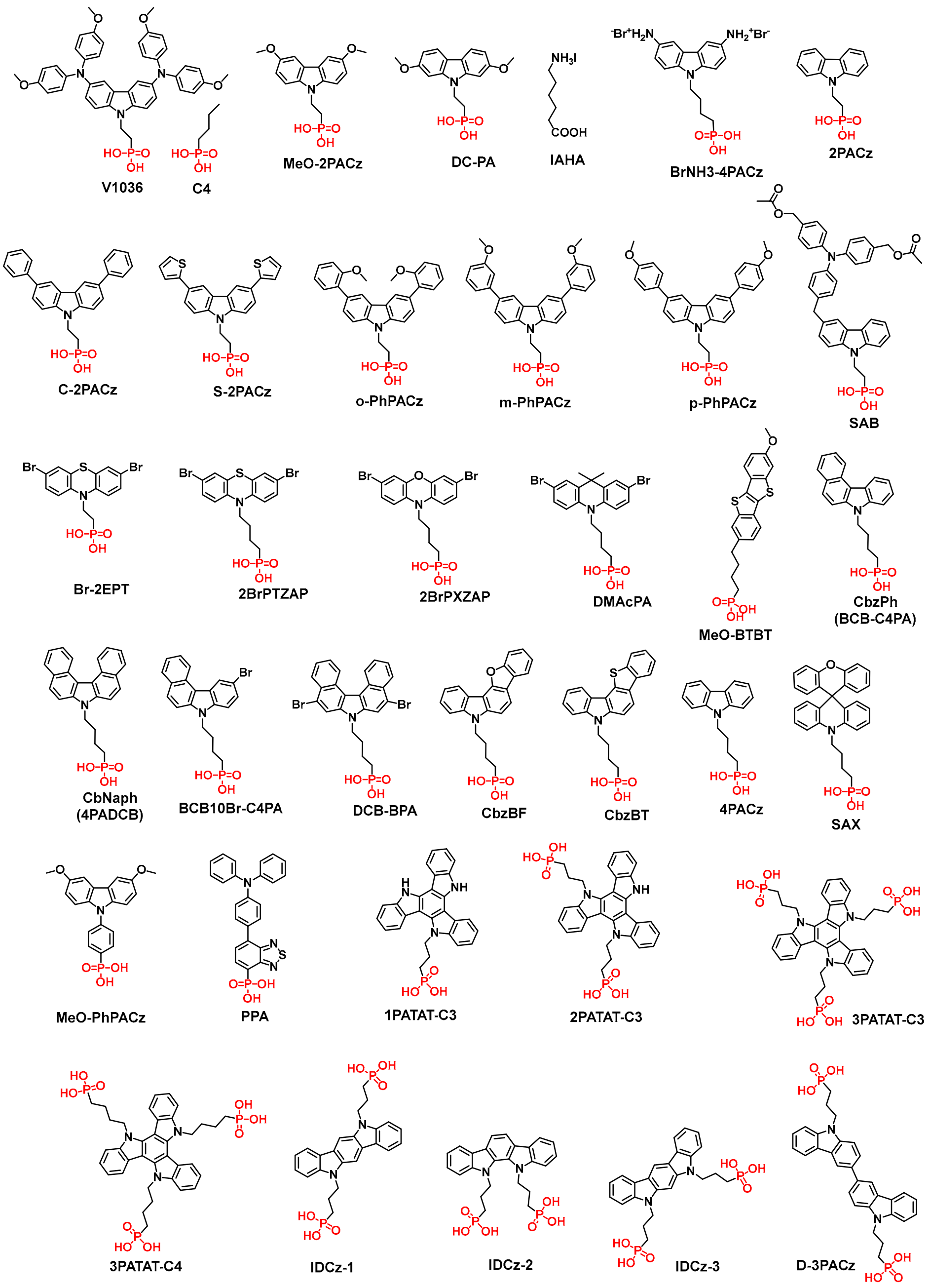

**Figure 4.** SAMs anchored with phosphonic acid.

Building upon the MeO-2PACz framework, Zhumagali et al. [68] developed $BrNH_3$-4PACz through Bromo ammonium modification. This novel molecule features a carbazole head group connected via an alkyl phosphonic acid anchoring group, which creates an optimal dipole moment at the ITO electrode surface. This configuration enables favorable energy level alignment, thereby significantly enhancing hole extraction efficiency from the narrow-bandgap (NBG) perovskite. Furthermore, the ionic Bromo ammonium moiety on the carbazole head group serves dual functions: effectively passivating defects at the perovskite bottom surface and regulating crystal growth during perovskite formation (Figure 4a). When integrated into an inverted p-i-n NBG PSCs (bandgap 1.24 eV), the device achieved a remarkable PCE of 23.0% with an open-circuit voltage ($V_{OC}$) of 0.88 V （Figure 4b). This performance ranks it among the highest-performing NBG PSCs reported to date (Figure 4c).

Building upon the MeO-2PACz framework, Zhumagali et al. [68] developed $BrNH_3$-4PACz through Bromo ammonium modification. This novel molecule features a carbazole head group connected via an alkyl phosphonic acid anchoring group, which creates an optimal dipole moment

at the ITO electrode surface. This configuration enables favorable energy level alignment, thereby significantly enhancing hole extraction efficiency from the narrow-bandgap (NBG) perovskite. Furthermore, the ionic Bromo ammonium moiety on the carbazole head group serves dual functions: effectively passivating defects at the perovskite bottom surface and regulating crystal growth during perovskite formation (Figure 5a). When integrated into an inverted p-i-n NBG PSCs (bandgap 1.24 eV), the device achieved a remarkable PCE of 23.0% with an open-circuit voltage ($V_{OC}$) of 0.88 V（Figure 5b). This performance ranks it among the highest-performing NBG PSCs reported to date (Figure 5c).

Similar to the HTLs in formal PSCs, molecular properties can also be optimized by extending molecular conjugation length [69]. In 2024, Wan et al. [70] introduced additional benzene rings or thiophene to 2PACz to prepare C-2PACz and S-2PACz. Compared with 2PACz, the incorporation of benzene rings and thiophene significantly enhanced the dipole moment of SAMs. This structural modification effectively regulated the work function of indium tin oxide (ITO) electrodes and achieved favorable energy level alignment with the perovskite light-absorbing layer. Due to electrostatic interactions between sulfur atoms in thiophene and undercoordinated $Pb^{2+}$ ions in perovskite, both C-2PACz and S-2PACz demonstrated enhanced defect passivation capabilities at perovskite interfaces. The two materials improved conductivity through reinforced conjugation effects, effectively promoting charge transport. Furthermore, the C-2PACz and S-2PACz-based HTLs served as crystallization templates for perovskite layers, resulting in more compact and uniform grains and higher-crystallinity films. Compared with 2PACz-based control devices, solar cells employing C-2PACz and S-2PACz exhibited reduced non-radiative recombination losses, higher power conversion efficiencies (18.1% and 18.65% respectively), and significantly improved device stability. Wu et al. [71] synthesized o-PhPACz, m-PhPACz, and p-PhPACz by introducing methoxy groups at different positions (ortho, meta and para) of the benzene ring based on C-2PACz. These functional groups not only significantly increased binding sites with the perovskite layer but also effectively regulated the molecular dipole moments. Among the series of SAMs, the meta-substituted m-PhPACz demonstrated optimal performance: it achieved a maximum dipole moment of 2.4 Debye, while the oxygen-oxygen spacing in the molecule showed an exact match with the diagonal spacing of adjacent lead ions in the perovskite lattice. This precise molecular design substantially enhanced the SAM-perovskite interfacial interaction, facilitating efficient charge transport while significantly improving interfacial stability. Consequently, m-PhPACz-based PSCs attained a PCE of 26.2% (a 12.9% improvement over the baseline) alongside exceptional environmental stability, retaining 96% of initial efficiency after 1000-hour thermal aging at 85°C and maintaining 90% efficiency retention after 300-hour UV irradiation.

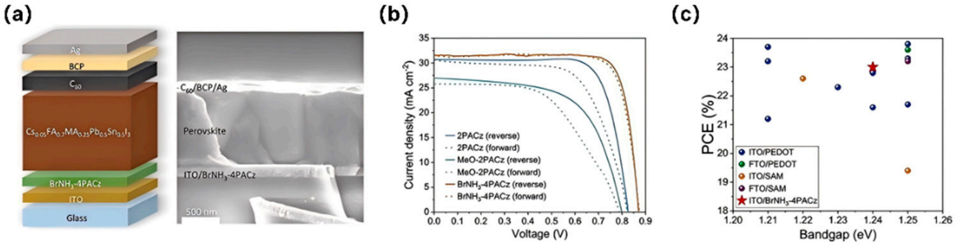

**Figure 5.** (a) Device architecture and cross-sectional SEM image of narrow bandgap p-i-n solar cells; (b) *J*–*V* scans of narrow bandgap single-junction solar cells fabricated on different ITO/SAM HTLs; (c) literature summary of PCE of narrow bandgap devices fabricated on different HTLs over the last 4 years. Copyright 2025 Wiley-VCH GmbH.

Dong et al. [72] synthesized SAB by connecting phosphorylated SAMs with triphenylamine. SAB not only exhibits excellent thermal stability, maintaining integrity without degradation for 200 hours at 100°C, but also demonstrates strong adhesion energy, which is 1.7 times higher than that of traditional SAMs-perovskite interfaces. The PSCs fabricated using SAB achieved a PCE exceeding

Preprints.org (www.preprints.org) | NOT PEER-REVIEWED | Posted: 6 May 2025 doi:10.20944/preprints202505.0128.v1

26% (certified efficiency), with champion devices showing exceptional performance under harsh environmental testing: they retained over 96% of their initial efficiency after 2,000 hours of damp-heat aging at 85°C and 85% relative humidity, and experienced less than 3% efficiency loss after 1,200 thermal cycling tests between -40°C and 85°C.

In addition to carbazole units, the end groups of SAMs can also use other donor structures. Ullah et al. [55] synthesized a promising new SAM Br-2EPT based on phenothiazine (PTZ) unit and used it as a hole selective contact for p-i-n PSCs. It can form a good energy interface bond with the perovskite absorber and minimize the non-radiative interface recombination loss, thus significantly improving charge extraction and device performance. The resulting PSCs have a high PCE of up to 22.44%, along with excellent operational stability. In 2023, He et al. [73] synthesized 2BrPTZPA, and 2BrPXZPA using bromo-substituted phenothiazine and phenoxazine (PXZ) as terminal groups. Due to the stronger electron-donation, non-planar configuration and presence of lone pairs of electrons of PTZ and PXZ, the devices based on 2BrPTZPA and 2BrPXZPA have more matched energy levels, lower charge complex losses and trap densities, and achieve high PCEs of 22.06% and 22.93%, respectively (certified PCE of 22.38%). In addition, the 2BrPXZPA-based PSC devices exhibit excellent stability. Furthermore, He et al. [74] regulated the structure of the terminal group and reported DMAcPA based on bromo dimethyl acridine. The two methyl groups in the end group aim to establish spatial effects to prevent aggregation at grain boundaries during film formation and to reduce the generation of complex centers. The molecule acted as an HTL to construct a good energy level match and achieve full passivation of the perovskite and grain boundaries, obtaining an optimal PSC with a PCE of 25.86%. Recently, Jen et al. [75] synthesized a SAM named MeO-BTBT with 7-methoxybenzo[b]benzo [4,5]thieno[2,3-d]thiophene as the terminal group. Compared to MeO-2PACz, MeO-BTBT has higher planarity and stronger conjugation, which enhances intermolecular interactions. Meanwhile, the sulfur atoms in MeO-BTBT can coordinate with $Pb^{2+}$ ions, which can passivate the defects at the buried interface of perovskite. As a result, the MeO-BTBT-based PSC achieved a high FF of 85.3% and a PCE of 24.53%.

Expanding the conjugation of terminal functional groups is also an effective strategy to improve the performance of SAMs. Jen et al. [76] prepared CbzPh and CbzNaph via asymmetric or helical $\pi$-extended carbazole units, and they concluded that this $\pi$-extended design not only improves the molecular dipole moments, but also enhances the $\pi$-$\pi$ interactions. The helical $\pi$-extended CbzNaph has a large dipole moment and forms a dense and ordered monolayer film. This modulates chalcogenide crystallization and optimizes the ITO functional. As a result, PSC with CbzNaph obtained 24.1% PCE and improved stability. Tang et al. [77] introduced bromine on the above mentioned asymmetric $\pi$-extended carbazole of CbzPh (BCB-C4PA) to obtain BCB10Br-C4PA. It was shown that the molecule has higher transmittance and lower energy levels compared to PTAA, which enhances interfacial charge transport and suppresses non-radiative recombination losses. Excellent performances have been exhibited in wide bandgap (WBG) PSCs and all-perovskite tandem solar cells (TSCs) based on BCB10Br-C4PA, as well as in bulk heterojunction OSCs. Tang's group [78] also further obtained DCB-BPA by symmetrically introducing bromine on the CbzNaph (4PADCB) of helical $\pi$-expanded carbazole, which has a significantly lower HOMO compared to PTAA, matches well with the perovskite energy levels, suppresses carrier nonradiative recombination at the interface, and promotes the subsequent growth of wide-bandgap perovskite and enhances the inter-interfacial interactions. The certified $V_{OC}$ of WBG PSCs based on DCB-BPA reached 1.339 V, resulting in a PCE of 18.88%. Besides, the PCE of DCB-BPA-based TSCs is up to 26.9%.

Recently, Jen's group [79] designed and synthesized two new multifunctional SAMs: CbzBF and CbzBT by introducing Lewis basic oxygen and sulfur heteroatoms through asymmetric molecular design (Figure 6a). It was experimentally demonstrated that these two SAMs could enhance the filling, modulate the work function of ITO, and passivate the defects at the buried interface of perovskite (Figure 6b). Finally, the champion PSC based on CbzBT achieved a PCE of 24.04%, an FF of 84.41% and excellent stability. In addition, this work demonstrated the feasibility of introducing passivation groups into high-performance SAMs. Based on 4PACz, Zhou et al. [80] synthesized a

SAM (SAX) featuring an orthogonal π-skeleton structure, exhibiting markedly enhanced tolerance to external stimuli over conventional conjugated molecular frameworks. SAX forms a unique disordered amorphous structure that not only exhibits high stability but also exceptional charge selectivity and transport properties. PSCs fabricated using SAX showed breakthrough long-term stability in accelerated aging tests, achieving a 23% improvement in open-circuit voltage retention compared to conventional systems. The devices retained 92% of their initial efficiency after 1000 hours of continuous operation under harsh 85°C/85% RH conditions. The champion SAX-based device achieved a PCE of 25.1%, with an FF of 83.4% and a $V_{OC}$ of 1.17 V.

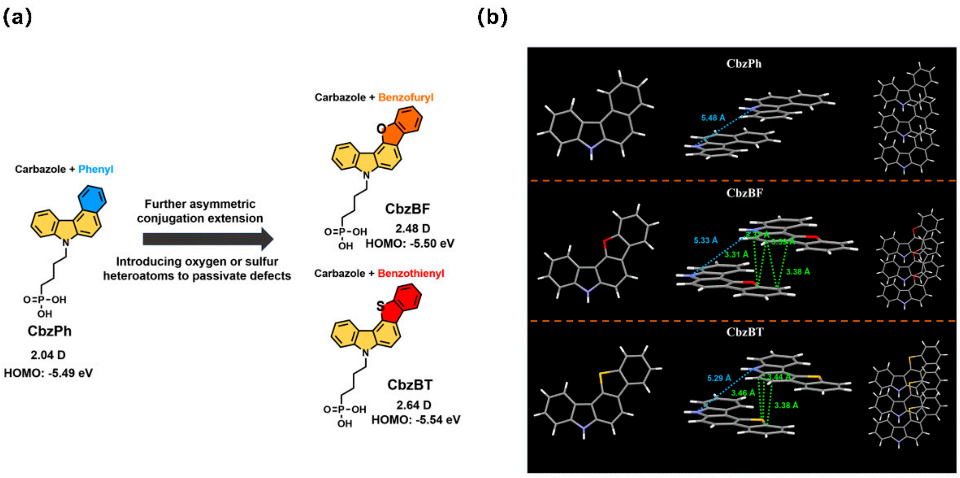

**Figure 6.** (a) Molecular structures, calculated dipole moments and HOMO energy levels of CbzPh, CbzBF, and CbzBT; (b) The molecular packing patterns in single crystals of the π-scaffolds of CbzPh (7*H*-benzo[*c*]carbazole), CbzBF (5*H*-benzofuro[3,2-*c*]carbazole), and CbzBT (5*H*-benzo[4,5]thieno[3,2-*c*]carbazole). Copyright 2024 The Royal Society of Chemistry.

The linkers of SAMs mentioned above are all alkyl chains, and it is also feasible to design SAMs using other linkers, such as benzene and benzothiadiazole. In 2023, Peng Gao et al. [81] synthesized MeO-PhPACz by replacing the linker of MeO-2PACz with a benzene ring. Compared with MeO-2PACz, the modification of the benzene ring led to a significant increase in the dipole moment and work function of the substrate. In addition, the benzene ring linker promotes the formation of a dense and highly ordered monomolecular layer on the substrate, which plays a key role in facilitating the growth of homogeneous perovskite films. As a consequence, a high PCE of 21.1% was obtained with a WBG PSC of 1.68 eV based on MeO-PhPACz. Li et al. [82] designed and synthesized PPA molecules by introducing benzothiadiazole as a linking unit into SAMs. The benzothiadiazole and the terminal triphenylamine group in PPA formed a D-A type structure to achieve efficient hole extraction and transport, and the PCE of PPA-based devices reached 23.24%.

The number of anchoring groups is a critical parameter for regulating the structure and performance of SAMs. In 2023, the Wakamiya team investigated the influence of anchoring group density on molecular adsorption behavior at TCO substrate surfaces by designing a multidentate molecular strategy [83]. They synthesized SAMs molecules with varying numbers of phosphonic acid groups and different alkyl chain lengths (3PATAT-C3, 2PATAT-C3, 1PATAT-C3, 3PATAT-C4) to study structure-property relationships. Results revealed that tridentate 3PATAT-C3 molecules, adopting a parallel substrate-aligned configuration, effectively optimized hole transport pathways and demonstrated superior charge recombination suppression compared to mono- or bidentate analogues. PSCs fabricated with 3PATAT-C3 achieved a PCE of 23.0% with excellent operational stability under continuous illumination. Conversely, extending the linker group from propyl (C3) to butyl (C4) increased intermolecular steric hindrance, impeding charge transport and reducing device efficiency. Wu et al. [84] designed three bisphosphonic acid-anchored IDCz-derived SAMs (IDCz-1, IDCz-2, IDCz-3; Figure 7a) by tuning the relative positions of dual nitrogen atoms in indolocarbazole

(IDCz) units. The ITO/IDCz-3/perovskite interface exhibited pronounced upward band bending with minor band offsets (Figure 7b), enhancing hole extraction efficiency while blocking electron back-recombination. Inverted PSCs based on IDCz-3 achieved a PCE of 25.15%, with unencapsulated devices retaining 95% initial performance after 1800-hour storage under ambient conditions. In 2024, Su et al. [85] developed a bisphosphonic acid-anchored SAMs molecule, D-3PACz. This material not only improved NiO$_x$ surface properties and energy-level alignment for enhanced hole extraction but also regulated perovskite crystal growth through strong interfacial interactions. D-3PACz-based PSCs exhibited reduced non-radiative recombination losses and defect densities, achieving a PCE of 23.8% and retaining 97% initial efficiency after 150 h of continuous illumination.

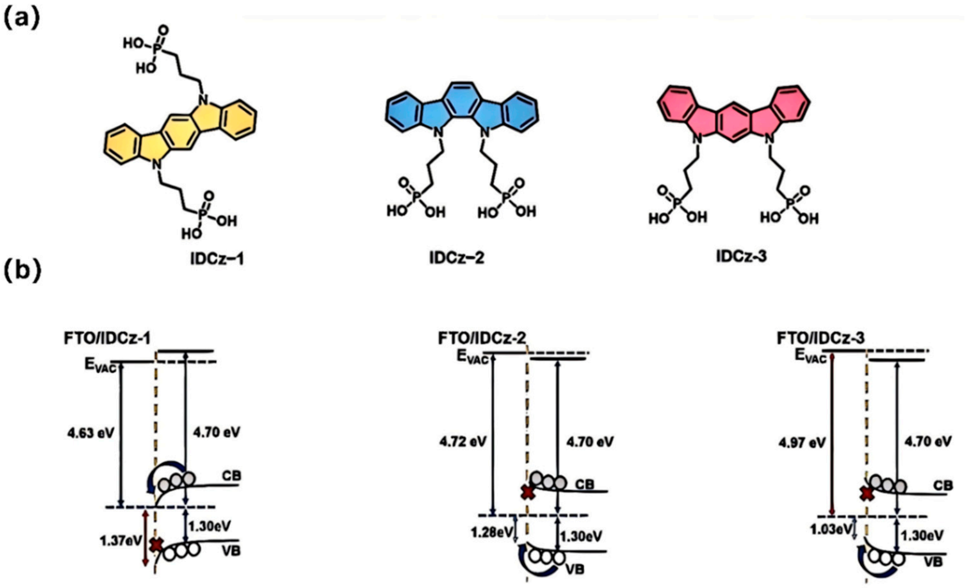

**Figure 7.** (a) Molecular structures of the indolocarbazole-derived SAMs. (b) Energy-level diagrams for FTO/IDCz-1/perovskite, FTO/IDCz-2/perovskite, and FTO/IDCz-3/perovskite. Copyright 2024 Wiley-VCH GmbH.

### *4.2. SAMs Anchored with Carboxylic Acid*

SAMs employing carboxylic acid as the anchoring group are also widely reported in existing studies. The corresponding molecular structures are illustrated in Figure 8, with their device performances detailed in Table 2.

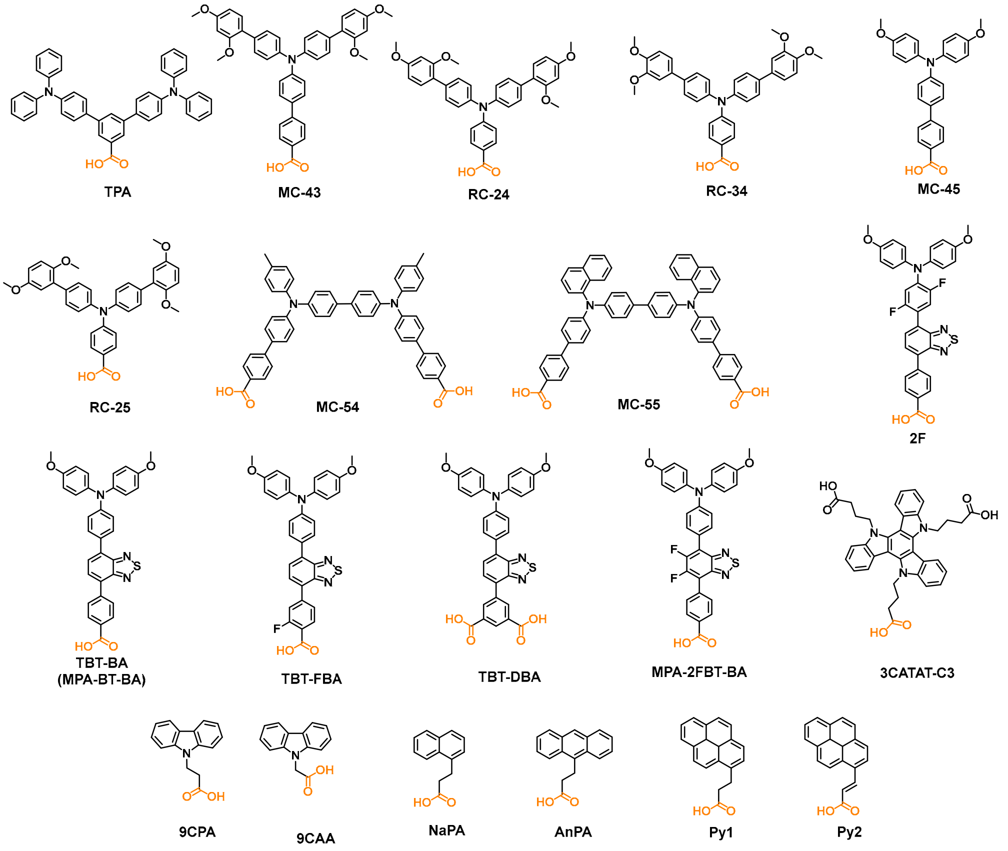

**Figure 8.** SAMs anchored with carboxylic acid.

In 2018, Palomares et al. [86] synthesized two SAMs (TPA and MC-43) with triphenylamine derivatives as terminal groups and carboxylic acid as an anchoring group, of which the MC-43-based PSC obtained a PCE of 17.3%. In 2022, they investigated the effect of terminal methoxy substitution position on SAMs and developed RC24, RC25, and RC34 by changing the position of methoxy on the molecular structure [87]. PSCs based on all three SAMs achieved PCEs nearly 20%. It is found that perovskites deposited on RC24 substituted by para- and ortho-substitutions could form large-grained films and thus enhanced PCE. Besides, Density-functional theory calculates suggested that the para- and ortho-substituted SAMs may form a well-ordered structure by improving the alignment of the SAMs, thus enhancing their stability on ITO. Recently, Palomares et al. [88] prepared MC-45 containing monocarboxylic acid and MC-54 and MC-55 containing dicarboxylic acid, in which the SAM of dicarboxylic acid has better charge transport ability, resulting in better device performance.

In 2023, Zhao's team [89] developed a D-A-type molecular material, MPA2FPh-BT-BA(2F), and successfully applied it as an HTL in both wide-bandgap and narrow-bandgap PSCs. In wide-bandgap devices, 2F exhibited efficient hole extraction capability and passivation of interfacial defects, effectively suppressing non-radiative recombination. In narrow-bandgap devices, 2F not only minimized interfacial energy loss but also regulated the crystal growth of Sn-Pb perovskites to enhance film quality. The study showed that 2F-optimized wide-bandgap devices achieved a PCE of 19.33% (independently certified 19.09%), while narrow-bandgap devices reached a PCE of 23.24%. Subsequently, Zhou's team [90] further optimized 2F to develop three novel SAMs: TBT-BA, TBT-FBA, and TBT-DBA. Their research revealed that TBT-BA, with the simplest molecular structure, formed the densest SAMs on $NiO_x$ surfaces, optimizing the $NiO_x$/SAMs/perovskite interface. This interface enhanced charge collection efficiency while passivating perovskite defects and suppressing interfacial reactions and carrier recombination. TBT-BA-based inverted PSCs achieved a champion PCE of 24.8% and retained 88.7% of their initial efficiency after 2635 hours in a 60°C glovebox environment. In the same year, Sun et al. [91] employed a distinct strategy to modify 2F, synthesizing two new SAMs: MPA-BT-BA (identical to TBT-BA) and MPA-2FBT-BA (Figure 9a). Results demonstrated that fluorinated MPA-2FBT-BA exhibited a lower HOMO level, higher hole mobility, enhanced hydrophobicity, and stronger interfacial interaction with the perovskite active layer compared to non-fluorinated MPA-BT-BA (Figure 9b-c). Perovskite layers in MPA-2FBT-BA-based PSCs displayed higher crystallinity and more uniform morphology, characterized by enlarged grain sizes and reduced non-radiative recombination. PSCs using MPA-2FBT-BA as the HTL achieved a PCE of 20.32% and demonstrated exceptional stability: unencapsulated devices retained 93% of their initial efficiency after 116 days in a nitrogen glovebox, and exhibited less than 9% efficiency degradation after 43 days of continuous exposure to air with 30±5% relative humidity, highlighting remarkable moisture resistance.

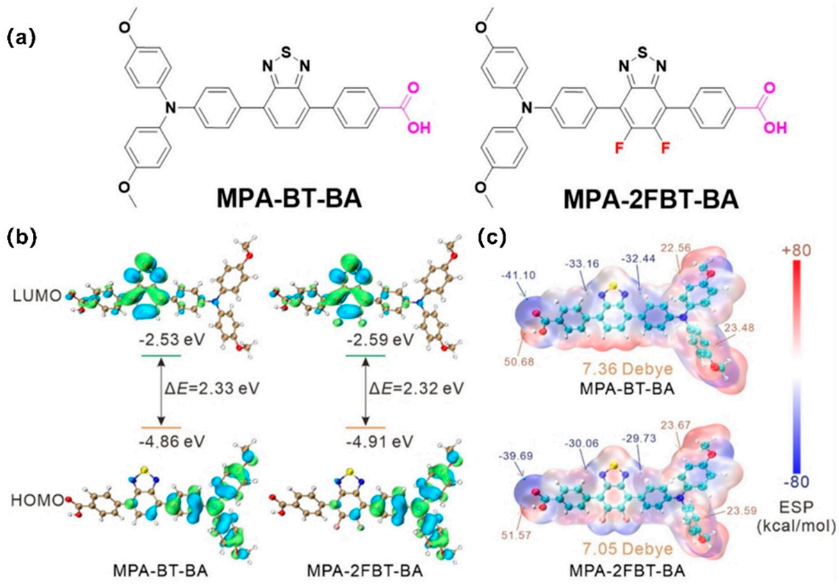

**Figure 9.** (a) Molecular structures of MPA-BT-BA and MPA-2FBT-BA; (b)The calculated distributions and energy levels of HOMO and LUMO in MPA-BT-BA and MPA-2FBT-BA; (c) The calculated electrostatic potential surface and dipole moment of MPA-BT-BA and MPA-2FBT-BA. Copyright 2024 Wiley-VCH GmbH.

In 2025, Truong et al. [92] developed a tripodal carboxylic acid-based SAM, termed 3CATAT-C3. Compared to its phosphonic acid-containing tripodal analog (3PATAT-C3), the 3CATAT-C3 molecules formed hydrophilic monolayers on transparent conductive oxide (TCO) surfaces, facilitating perovskite film deposition in conventional layer-by-layer fabrication processes. Notably, its larger diffusion coefficient and higher surface energy enabled 3CATAT-C3 to be compatible with simplified, low-cost one-step co-deposition processes. After spin-coating, 3CATAT-C3 preferentially accumulated at the bottom interface of the perovskite film, effectively enhancing charge extraction efficiency. 3CATAT-C3-incorporated PSCs fabricated via co-deposition demonstrated outstanding performance, achieving a record PCE exceeding 23%. Unencapsulated devices exhibited excellent stability, retaining 90% of their initial performance after 100 hours of operation, preserving 95% of their initial efficiency after heating in air at 105°C, and showing no performance degradation during 8000 hours of storage.

In 2024, Li's team reported novel SAMs with carbazole terminal groups and carboxylic acid anchoring groups, termed 9CPA and 9CAA [93] . Studies revealed that compared to traditional phosphonic acid-anchored SAMs, carboxylic acid-modified SAMs achieved a more ordered molecular orientation on conductive substrates. This ordered structure strengthened molecular interactions with perovskites, effectively suppressing non-radiative recombination and enhancing the crystallinity of perovskite films. Additionally, the short-chain linkers optimized energy level alignment between the SAMs and perovskite layers, thereby improving hole extraction efficiency. Ultimately, PSCs fabricated with 9CAA achieved a PCE of 23.1%. To investigate the impact of $\pi$-conjugation on the PCE and stability of PSCs, Zhao et al. [94] synthesized a series of SAMs with extended $\pi$-conjugated structures: NaPA、AnPA、 Py1 and Py2. Their research demonstrated that as the π-conjugation of the molecules expanded, the SAMs progressively enhanced hole extraction/transport efficiency and improved device performance. Concurrently, strengthened intermolecular π-π interactions significantly boosted the stability of PSCs. Py2, the structurally optimized molecule in the series, yielded PSCs with a remarkable PCE of 25.2% and outstanding stability.

### *4.3. SAMs Anchored with Cyanoacetic Acid*

Cyanoacetic acid was used as an anchoring group of SAMs in PSCs with equally good results, the molecular structure is shown in Figure 10, and the device parameters are listed in Table 3.

In 2020, Guo et al. [95] prepared a D-A type SAM, named MPA-BT-CA. Due to the introduction of cyanoacetic acid, MPA-BT-CA are not only able to effectively regulate the orbital energy levels of the frontier molecules, but also modify the interfaces of the ITO electrodes, effectively passivate defects in the perovskite layer, and have a good solubility for alcohols. The MPA-BT-CA based PSCs achieved 21.24% PCE and has good long-term stability under ambient conditions. In addition, when the MPA-BT-CA films were treated with the green solvent ethanol, the corresponding PSCs also exhibited a PCE of 20.52%.

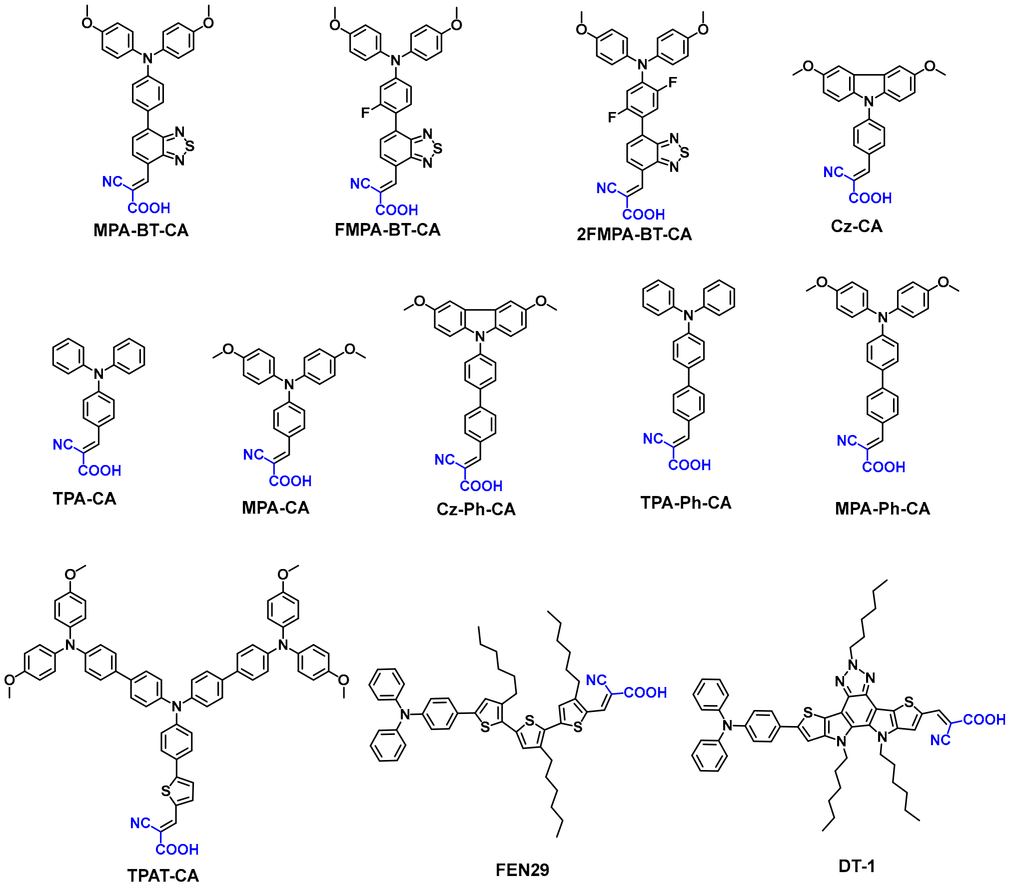

**Figure 10.** SAMs anchored with cyanoacetic acid.

This group further reported two SAMs FMPA-BT-CA (1 F) and 2FMPA-BT-CA (2 F) using fluorination strategy [56]. The fluorination strategy can improve the optoelectronic and film surface properties of the SAMs. First, a deeper HOMO energy level is obtained, which can well match the valence band of the perovskite layer. Second, FMPA-BT-CA and 2FMPA-BT-CA have higher dipole moments compared to the fluorine-free MPA-BT-CA, thus favoring carrier extraction. Thirdly, the fluorinated SAMs have a significant passivation effect on perovskite, thus allowing the formation of high-quality perovskite films. The FMPA-BT-CA-based devices treated with green solvent (isopropanol) achieved 22.37% PCE and good photostability.

In 2022, Zhu et al. [96] reported a series of conjugated SAMs Cz-CA, TPA-CA, MPA-CA, Cz-Ph-CA, TPA-Ph-CA, and MPA-Ph-CA with excellent photostability and electrical stability (Figure 11a). The conjugated molecular structure not only enhances charge transport but also stabilizes electron-rich aromatic amines through electron/charge delocalization. In addition, it can conveniently modulate the frontier orbital energy levels for interfacial energy level matching (Figure 11 b). Ultimately, the PSC based on the optimally conjugated MPA-Ph-CA achieved a PCE of 22.53% (certified as 22.12%) and good stability.In 2024, Afraj et al. [97] synthesized a Y-shaped TPA-based SAMs molecule (TPAT-CA) for tin-based PSCs, where the thiophene group facilitated the formation of tin-based perovskite nanocrystals with superior morphology, crystallinity, and surface roughness. The Y-shaped structure enhanced hole mobility and suppressed charge recombination. The TPAT-CA-based tin-based PSCs achieved a PCE of 8.1% and exhibited exceptional stability, retaining 90% of their initial efficiency after 3000 hours of storage.

Cheng's team developed two D-π-A-structured SAMs (FNE29 and DT-1) as HTLs for inverted PSCs, modifying ITO substrates via covalent self-assembly [98]. FNE29 employed a hexyl-substituted terthiophene π-bridge, while DT-1 utilized a fused-ring system (dithienopyrrolobenzotriazole) as the linking group, leading to significant performance differences. SAMs-modified devices showed remarkable improvements: the control device (unmodified) had a PCE of 9.36%, which increased to 16.75% for FNE29 and 20.65% for DT-1. This enhancement was attributed to DT-1's large conjugated fused-ring π-bridge, which improved hole transport and yielded a higher fill factor. Additionally, the hydrophobic nature of both SAMs granted the devices excellent environmental stability: they retained over 80% of their initial efficiency after 1000 hours of unencapsulated storage in ambient air and demonstrated robust photostability under continuous illumination for 1000 hours.

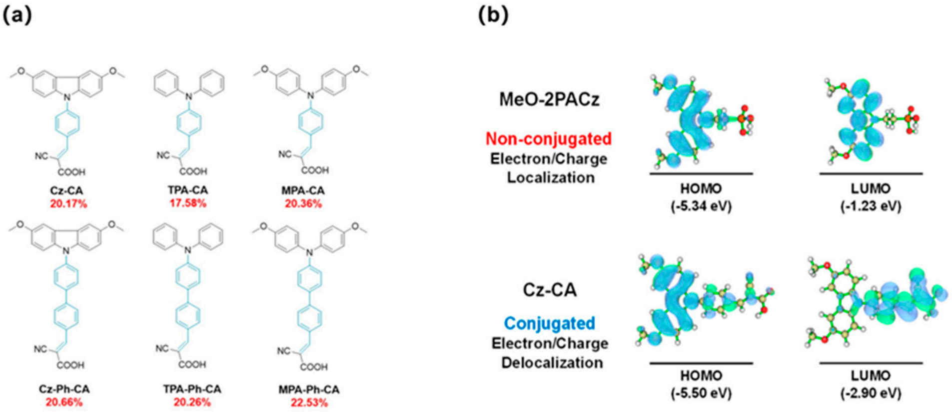

**Figure 11.** (a) conjugated SAMs developed in this work; (b) Mechanism of conjugated structure for improving the stability of SAMs. For alkyl-linker based SAMs, the isolated and localized electron-rich arylamine is prone to oxidation and the high LUMO level increases reaction activity of excited state species. In contrast, conjugated SAMs featuring delocalized electron distribution and stabilized LUMO level decrease the activity of both ground and excited states. Copyright 2022 American Chemical Society.

### *4.4. SAMs Anchored with Other Functional Groups*

Previous sections have introduced the commonly used anchoring groups for SAMs in PSCs. We now present SAMs synthesized with uncommon anchoring groups, as illustrated in Figure 12 and Table 4.

**Table 4.** The energy level of SAMs with other acid as the anchor group and their performance parameters in the PSCs.

| SAMs | HOMO （eV） | Device structure | $V_{OC}$ (V) | $J_{SC}$ (mA/cm$^2$) | FF(%) | PCE(%) | Ref |
|---|---|---|---|---|---|---|---|

| | | | | | | | |
|---|---|---|---|---|---|---|---|
| **MTPA-BA** | -5.48 | ITO/MTPA-BA/$Cs_{0.05}(FA_{0.95}MA_{0.05})_{0.95}Pb(I_{0.95}Br_{0.05})_3$/PCBM/$C_{60}$/BCP/Ag | 1.14 | 23.24 | 85.2 | 22.62 | [99] |
| **MPA-CAP** | -5.4 | ITO/MPA-CAP/$Cs_{0.05}(FA_{0.95}MA_{0.05})_{0.95}Pb(I_{0.95}Br_{0.05})_3$/F-PEAI/$C_{60}$/BCP/Ag | 1.21 | 24.78 | 84.7 | 25.4 | [37] |
| **XS8** | -5.53 | ITO/ XS8/perovskite/PCBM/BCP/Ag | 1.05 | 21.29 | 73.16 | 16.11 | [100] |
| **XS9** | -5.49 | ITO/ XS9/perovskite/PCBM/BCP/Ag | 1.02 | 22.27 | 71.32 | 15.77 | [100] |
| **XS10** | -5.37 | ITO/ XS10/perovskite/PCBM/BCP/Ag | 1.09 | 22.71 | 81.85 | 20.28 | [100] |

As an acidity-weakened acid, boric acid can also be used as the anchor group of SAM. Wu et al. [99] reported a SAM MTPA-BA with boric acid as the anchor group to construct efficient SAM-based hole-selective contact (HSC) for PSCs. Theoretical evaluation revealed that boric acid spontaneously chemisorbs onto indium tin oxide (ITO) surface with oxygen vacancies facilitating the adsorption progress. Spectroscopy and electrical measurements indicate that boric acid anchor significantly mitigates ITO corrosion. Besides, a certain amount of free boric acid containing SAMs improves perovskite deposition and results in a coherent and well-passivated bottom interface, which boosts the fill factor (FF) performance for a variety of perovskite compositions. As a result, the optimal PSC based on MTPA-BA obtained PCE close to 23% with a high FF of 85.2%. More importantly, PSCs based on MTPA-BA show better stability than those based on SAM with phosphonic acid anchoring groups, indicating the huge potential of boronic acid anchoring groups for passivating interfaces and improving device stability.

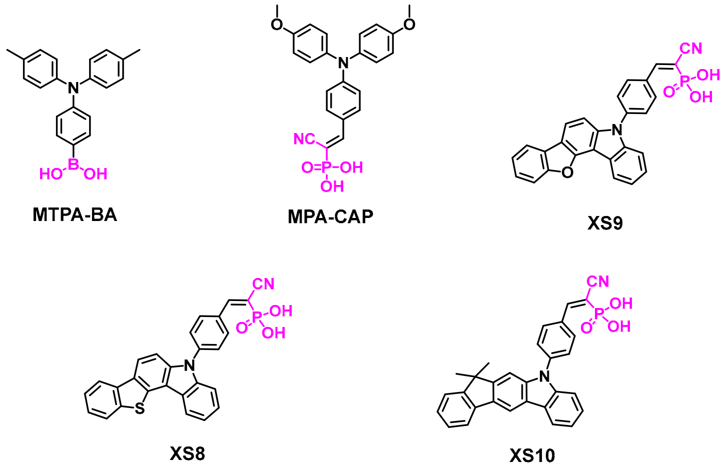

**Figure 12.** SAMs anchored with another anchor group.

The cyanovinyl phosphonic acid group has good hydrophilicity and can be used as an anchoring group for SAMs in PSCs to demonstrate excellent performance. Wu et al. [37] reported an amphiphilic molecular hole transporter MAP-CAP with cyanovinyl phosphonic acid as an anchoring group. Due to the introduction of multifunctional hydrophilic cyano phosphonic acid, MPA-CPA can be soluble in high and low polarity solvents. In addition, it minimizes interfacial defects, resulting in high-quality perovskite films. As a result, the MAP-CAP-based PSCs showed a certified PCE of 25.4%. Moreover, PCEs of 23.4% and 22.0% were achieved in 1–square centimeter cells and 10–square centimeter minimodules, respectively, with good stability. Guo et al. [100] proposed constructing novel fused carbazole-based SAMs by extending the π-conjugated system of carbazole units. They designed and synthesized three SAMs molecules—XS8, XS9, and XS10. These new SAMs feature a highly rigid and planar fused carbazole as the terminal group and a conjugated alkene linkage unit. This conjugated structural expansion effectively enhanced molecular planarity, stability, and dipole moment（Figure 13）. Among them, XS10, with the largest conjugated system, demonstrated the best

doi:10.20944/preprints202505.0128.v1

performance in perovskite devices. XS10-based PSCs achieved a PCE of 20.28%, significantly surpassing the 17.19% PCE of classical 2PACz-based devices.

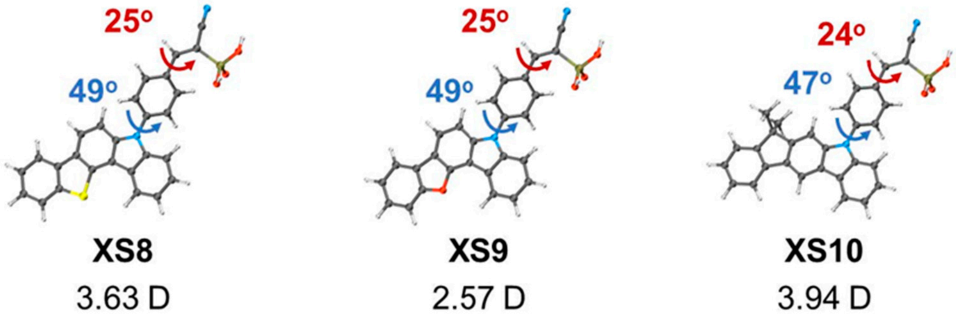

**Figure 13.** The optimized geometric molecular configuration and dipole moments of SAMs. Copyright 2024 Wiley-VCH GmbH.

## 5. Conclusions and Perspectives

The application of SAMs has improved the performance of p-i-n PSCs by leaps and bounds and injected new vigor into the development of PSCs. Due to its advantages of flexible structure, low material consumption and easy processing, it has been widely used as an HTL, demonstrating good application prospects. We have classified and categorized the SAM-HTLs through the differences in both the types of anchoring groups and the number of anchoring groups in SAMs, and discussed in detail the relationship between the SAMs structures and their chemical-physical properties, as well as the effects of the SAMs structures on the PSCs.

Although SAMs show great potential in PSCs, their commercial applications still face some challenges. For example, how to achieve uniform deposition of SAMs over large areas and how to improve the stability and durability of SAMs still need further investigation. We envision that future SAM development will be based on the following two aspects to accelerate the commercialization of perovskite solar cells: design of molecular structure and device commercial production.

### *5.1. Design of Molecular Structure*

The SAM is mainly composed of an anchoring group, a linker unit and a terminal group. Although excellent device performance and stability have been reported for SAM-based PSCs, the terminal donor groups of SAM molecules are dominated by structures such as carbazole, triphenylamine, phenothiazine, etc., and most of the connecting units are alkyl groups, benzene rings, and thiophene, which are relatively homogeneous molecular systems. Some excellent donor units in optoelectronic materials have not yet been introduced into the SAM structure, for example, indoline and fluorene units should also be able to be used as terminal groups of SAMs by rational molecular structure design. Besides, phosphonic, carboxylic, and cyanoacetic acids are commonly used as anchoring groups in the structure of SAMs, and SAMs with these anchoring groups exhibit excellent performance in PSCs. Currently, the anchoring groups in SAMs are mainly phosphoric acid, carboxylic acid and cyanoacetic acid, in addition, SAMs with boric acid and cyanovinyl phosphonic acid as anchoring groups have also been reported recently. SAMs with these anchoring groups have achieved excellent performances in chalcogenide solar cells. However, according to the development of photosensitive dye molecules in DSSCs, other excellent anchoring groups such as hydantoin, anhydrides, trimethyl silanes, etc., also have a great potential to be applied in SAMs. Currently, the main linkers of SAMs are alkyl and benzene rings, while other units such as pyridine, thiophene, furan and thiazole are expected to further enhance the properties of SAMs. The rational design of the three components of the SAM can help to improve the energy level matching between the HTL and the perovskite, reduce non-radiative recombination, lower the voltage loss and increase the open-circuit voltage and fill factor, thus enhancing the performance and stability of PSCs. In addition, the photothermal stability of SAMs is generally poor, which can lead to reduced device stability. How to improve the photothermal stability of SAMs by molecular design is an urgent problem.

### *5.2. Device Commercial Production*

The preparation of high-quality SAM films is one of the main factors affecting the commercialization of SAM-based PSCs. Ideally, high-performance PSCs can be realized by rational molecular design to achieve a dense and uniform film of SAM on the substrate; however, the backbones of the currently commonly used SAMs are easy to aggregate; in addition, the size of the SAMs is large, and the substrate still has vacancies that are not adsorbed by anchoring groups, which increases non-radiative recombination. Introducing the appropriate additives (e.g., surfactants, co-adsorbents, etc.) into the SAM solution improves the uniformity, crystalline quality, and performance of the film. These additives optimize the arrangement and distribution of the SAMs, thereby improving the overall quality of the film. At present, the spin-coating method is widely used in the laboratory and is clearly not suitable for the fabrication of large-area devices. The development of deposition processes suitable for commercial applications is key to the wide range of applications of SAMs.

In summary, the application of SAMs in PSCs has broad prospects and important research value. By continuously optimizing the structure of SAMs and developing new film preparation and deposition methods, the performance and stability of PSCs can be further improved, and their application and development in the field of renewable energy can be promoted.

**Author Contributions: Yajie Fu:** Writing–original draft, review & editing. **Chunguang Li:** Writing–original draft, review & editing. **Yang Li:** Writing–review & editing, Supervision, Project administration.

**Acknowledgments:** This work was financially supported by Project of Qinghai Science and Technology Department (Grant No. 2023-ZJ-975Q).

**Conflicts of Interest:** The authors declare no conflict of interest.

## Graphical Abstract

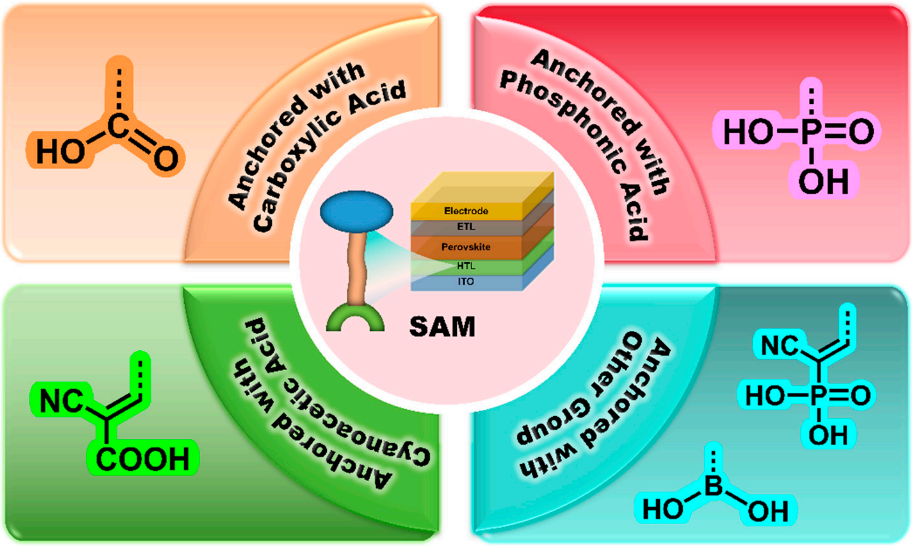

## References

1. Leijtens, T., Eperon, G. E., Pathak, S., Abate, A., Lee, M. M., Snaith, H. J. Overcoming ultraviolet light instability of sensitized TiO2 with meso-superstructured organometal tri-halide perovskite solar cells. *Nat. Commun.* **2013**, *4*, 2885. http://dx.doi.org/10.1038/ncomms3885.

2. Wang, T., Cao, X., Jiao, L. PEM water electrolysis for hydrogen production: fundamentals, advances, and prospects. *Carb Neutrality* **2022**, *1*, 21. http://dx.doi.org/10.1007/s43979-022-00022-8.
3. Albrahee, I., Li, Y., Xing, G. Carbon-based Perovskite Solar Cells: From Current Fabrication Methodologies to Their Future Commercialization at Low Cost. *Innov Discov* **2025**, *1*, 1. http://dx.doi.org/10.53964/id.2025001.
4. Yoo, J. J., Shin, S. S., Seo, J. Toward Efficient Perovskite Solar Cells: Progress, Strategies, and Perspectives. *Acs Energy Lett* **2022**, *7*, 2084-2091. http://dx.doi.org/10.1021/acsenergylett.2c00592.
5. Stranks, S. D., Eperon, G. E., Grancini, G., Menelaou, C., Alcocer, M. J. P., Leijtens, T., Herz, L. M., Petrozza, A., Snaith, H. J. Electron-Hole Diffusion Lengths Exceeding 1 Micrometer in an Organometal Trihalide Perovskite Absorber. *Sci* **2013**, *342*, 341-344. http://dx.doi.org/10.1126/science.1243982.
6. Kim, H.-S., Lee, C.-R., Im, J.-H., Lee, K.-B., Moehl, T., Marchioro, A., Moon, S.-J., Humphry-Baker, R., Yum, J.-H., Moser, J. E., Grätzel, M., Park, N.-G. Lead Iodide Perovskite Sensitized All-Solid-State Submicron Thin Film Mesoscopic Solar Cell with Efficiency Exceeding 9%. *Sci Rep* **2012**, *2*, 591. http://dx.doi.org/10.1038/srep00591.
7. National Renewable Energy Laboratory (NREL), Best Research-Cell Efficiencies. http://dx.doi.org/https://www.nrel.gov/pv/assets/pdfs/cell-pv-eff-emergingpv.pdf.
8. Luo, X., Lin, X., Gao, F., Zhao, Y., Li, X., Zhan, L., Qiu, Z., Wang, J., Chen, C., Meng, L., Gao, X., Zhang, Y., Huang, Z., Fan, R., Liu, H., Chen, Y., Ren, X., Tang, J., Chen, C.-H., Yang, D., Tu, Y., Liu, X., Liu, D., Zhao, Q., You, J., Fang, J., Wu, Y., Han, H., Zhang, X., Zhao, D., Huang, F., Zhou, H., Yuan, Y., Chen, Q., Wang, Z., Liu, S. F., Zhu, R., Nakazaki, J., Li, Y., Han, L. Recent progress in perovskite solar cells: from device to commercialization. *Sci. China Chem.* **2022**, *65*, 2369-2416. http://dx.doi.org/10.1007/s11426-022-1426-x.
9. Kojima, A., Teshima, K., Shirai, Y., Miyasaka, T. Organometal Halide Perovskites as Visible-Light Sensitizers for Photovoltaic Cells. *J. Am. Chem. Soc.* **2009**, *131*, 6050-6051. http://dx.doi.org/10.1021/ja809598r.
10. Kim, J. Y., Lee, J.-W., Jung, H. S., Shin, H., Park, N.-G. High-Efficiency Perovskite Solar Cells. *Chem. Rev.* **2020**, *120*, 7867-7918. http://dx.doi.org/10.1021/acs.chemrev.0c00107.
11. Pham, H. D., Yang, T. C. J., Jain, S. M., Wilson, G. J., Sonar, P. Development of Dopant-Free Organic Hole Transporting Materials for Perovskite Solar Cells. *Adv. Energy Mater.* **2020**, *10*, 1903326. http://dx.doi.org/10.1002/aenm.201903326.
12. Yang, S., Fu, W., Zhang, Z., Chen, H., Li, C.-Z. Recent advances in perovskite solar cells: efficiency, stability and lead-free perovskite. *J. Mater. Chem. A* **2017**, *5*, 11462-11482. http://dx.doi.org/10.1039/c7ta00366h.
13. Li, Y., Zhang, Q., Liu, L., Wang, D., Liu, Z., Yuan, N., Ding, J., Wang, Q., Liu, S. Multifunctional indaceno [1,2-b:5,6-b′]dithiophene chloride molecule for stable high-efficiency perovskite solar cells. *Sci. China Chem.* **2022**, *66*, 185-194. http://dx.doi.org/10.1007/s11426-022-1403-6.
14. Urieta-Mora, J., García-Benito, I., Molina-Ontoria, A., Martín, N. Hole transporting materials for perovskite solar cells: a chemical approach. *Chem. Soc. Rev.* **2018**, *47*, 8541-8571. http://dx.doi.org/10.1039/c8cs00262b.
15. Shao, J. Y., Zhong, Y. W. Low-Cost, High-Performance Organic Small Molecular Hole-Transporting Materials for Perovskite Solar Cells. *Chinese J Org Chem* **2021**, *41*, 1447-1465. http://dx.doi.org/10.6023/cjoc202009033.
16. Shao, J.-Y., Li, D., Shi, J., Ma, C., Wang, Y., Liu, X., Jiang, X., Hao, M., Zhang, L., Liu, C., Jiang, Y., Wang, Z., Zhong, Y.-W., Liu, S. F., Mai, Y., Liu, Y., Zhao, Y., Ning, Z., Wang, L., Xu, B., Meng, L., Bian, Z., Ge, Z., Zhan, X., You, J., Li, Y., Meng, Q. Recent progress in perovskite solar cells: material science. *Sci. China Chem.* **2022**, *66*, 10-64. http://dx.doi.org/10.1007/s11426-022-1445-2.
17. Sun, X., Zhao, D., Li, Z. a. Recent advances in the design of dopant-free hole transporting materials for highly efficient perovskite solar cells. *Chin. Chem. Lett.* **2018**, *29*, 219-231. http://dx.doi.org/10.1016/j.cclet.2017.09.038.
18. Tang, G., You, P., Tai, Q., Yang, A., Cao, J., Zheng, F., Zhou, Z., Zhao, J., Chan, P. K. L., Yan, F. Solution-Phase Epitaxial Growth of Perovskite Films on 2D Material Flakes for High-Performance Solar Cells. *Adv. Mater.* **2019**, *31*, 1807689. http://dx.doi.org/10.1002/adma.201807689.
19. Li, Y., Liao, J.-F., Pan, H., Xing, G. Interfacial Engineering for High-Performance PTAA-Based Inverted 3D Perovskite Solar Cells. *Sol. RRL* **2022**, *6*, 2200647. http://dx.doi.org/10.1002/solr.202200647.

20. Wang, Z., Dong, Q., Yan, Y., Fang, Z., Mi, G., Pei, M., Wang, S., Zhang, L., Liu, J., Chen, M., Ma, H., Wang, R., Zhang, J., Cheng, C., Shi, Y. Al2O3 nanoparticles as surface modifier enables deposition of high quality perovskite films for ultra-flexible photovoltaics. *Adv. Powder Mater.* **2024**, *3*, 100142. http://dx.doi.org/10.1016/j.apmate.2023.100142.
21. Gangala, S., Misra, R. Spiro-linked organic small molecules as hole-transport materials for perovskite solar cells. *J. Mater. Chem. A* **2018**, *6*, 18750-18765. http://dx.doi.org/10.1039/c8ta08503j.
22. Huang, W., Xie, L.-H., Sun, Y.-G., Ren, B.-Y., Liu, Q.-L. Research Progress of Hole Transport Materials Based on Spiro Aromatic-Skeleton in Perovskite Solar Cells. *Acta Chimica Sinica* **2021**, *79*. http://dx.doi.org/10.6023/a21060253.
23. Liu, X.-P., Kong, F.-T., Chen, W.-C., Yu, T., Guo, F.-L., Chen, J., Dai, S.-Y. Application of Organic Hole-Transporting Materials in Perovskite Solar Cells. *Acta Phys.-Chim. Sin.* **2016**, *32*, 1347-1370. http://dx.doi.org/10.3866/pku.Whxb201603143.
24. Fu, Y., Li, C., Zhao, Y., Cao, D. Dopant-free hole transport materials for perovskite solar cells: Isoindigo and dibenzonaphthyridine derivatives. *Dyes Pigments* **2025**, *235*. http://dx.doi.org/10.1016/j.dyepig.2024.112617.
25. Marinova, N., Tress, W., Humphry-Baker, R., Dar, M. I., Bojinov, V., Zakeeruddin, S. M., Nazeeruddin, M. K., Grätzel, M. Light Harvesting and Charge Recombination in CH3NH3PbI3 Perovskite Solar Cells Studied by Hole Transport Layer Thickness Variation. *ACS NANO* **2015**, *9*, 4200-4209. http://dx.doi.org/10.1021/acsnano.5b00447.
26. Meng, L., You, J., Guo, T.-F., Yang, Y. Recent Advances in the Inverted Planar Structure of Perovskite Solar Cells. *Acc. Chem. Res.* **2015**, *49*, 155-165. http://dx.doi.org/10.1021/acs.accounts.5b00404.
27. Chen, S., Dai, X., Xu, S., Jiao, H., Zhao, L., Huang, J. Stabilizing perovskite-substrate interfaces for high-performance perovskite modules. *Sci* **2021**, *373*, 902-907. http://dx.doi.org/10.1126/science.abi6323.
28. Sun, X., Li, Z., Yu, X., Wu, X., Zhong, C., Liu, D., Lei, D., Jen, A. K. Y., Li, Z. a., Zhu, Z. Efficient Inverted Perovskite Solar Cells with Low Voltage Loss Achieved by a Pyridine-Based Dopant-Free Polymer Semiconductor. *Angew. Chem. Int. Ed.* **2021**, *60*, 7227-7233. http://dx.doi.org/10.1002/anie.202016085.
29. Wang, S., Guo, H., Wu, Y. Advantages and challenges of self-assembled monolayer as a hole-selective contact for perovskite solar cells. *MF* **2023**, *2*, 012105. http://dx.doi.org/10.1088/2752-5724/acbb5a.
30. Isikgor, F. H., Zhumagali, S., T. Merino, L. V., De Bastiani, M., McCulloch, I., De Wolf, S. Molecular engineering of contact interfaces for high-performance perovskite solar cells. *Nat Rev Mater* **2022**, *8*, 89-108. http://dx.doi.org/10.1038/s41578-022-00503-3.
31. Cheng, H., Li, Y., Zhong, Y. Towards cost-efficient and stable perovskite solar cells and modules: utilization of self-assembled monolayers. *Mater. Chem. Front.* **2023**, *7*, 3958-3985. http://dx.doi.org/10.1039/d3qm00209h.
32. Puerto Galvis, C. E., González Ruiz, D. A., Martínez-Ferrero, E., Palomares, E. Challenges in the design and synthesis of self-assembling molecules as selective contacts in perovskite solar cells. *Chem. Sci.* **2024**, *15*, 1534-1556. http://dx.doi.org/10.1039/d3sc04668k.
33. Lan, Z.-R., Shao, J.-Y., Zhong, Y.-W. Self-assembled monolayers as hole-transporting materials for inverted perovskite solar cells. *Mol. Syst. Des. Eng.* **2023**, *8*, 1440-1455. http://dx.doi.org/10.1039/d3me00144j.
34. Ali, F., Roldán-Carmona, C., Sohail, M., Nazeeruddin, M. K. Applications of Self-Assembled Monolayers for Perovskite Solar Cells Interface Engineering to Address Efficiency and Stability. *Adv. Energy Mater.* **2020**, *10*, 2002989. http://dx.doi.org/10.1002/aenm.202002989.
35. Afraj, S. N., Kuan, C. H., Lin, J. S., Ni, J. S., Velusamy, A., Chen, M. C., Diau, E. W. G. Quinoxaline-Based X-Shaped Sensitizers as Self-Assembled Monolayer for Tin Perovskite Solar cells. *Adv. Funct. Mater.* **2023**, *33*, 2213939. http://dx.doi.org/10.1002/adfm.202213939.
36. Galoppini, E. Linkers for anchoring sensitizers to semiconductor nanoparticles. *Coord. Chem. Rev.* **2004**, *248*, 1283-1297. http://dx.doi.org/10.1016/j.ccr.2004.03.016.
37. Zhang, S., Ye, F., Wang, X., Chen, R., Zhang, H., Zhan, L., Jiang, X., Li, Y., Ji, X., Liu, S., Yu, M., Yu, F., Zhang, Y., Wu, R., Liu, Z., Ning, Z., Neher, D., Han, L., Lin, Y., Tian, H., Chen, W., Stolterfoht, M., Zhang, L., Zhu, W.-H., Wu, Y. Minimizing buried interfacial defects for efficient inverted perovskite solar cells. *Sci* **2023**, *380*, 404-409. http://dx.doi.org/10.1126/science.adg3755.

38. Park, S. M., Wei, M., Lempesis, N., Yu, W., Hossain, T., Agosta, L., Carnevali, V., Atapattu, H. R., Serles, P., Eickemeyer, F. T., Shin, H., Vafaie, M., Choi, D., Darabi, K., Jung, E. D., Yang, Y., Kim, D. B., Zakeeruddin, S. M., Chen, B., Amassian, A., Filleter, T., Kanatzidis, M. G., Graham, K. R., Xiao, L., Rothlisberger, U., Grätzel, M., Sargent, E. H. Low-loss contacts on textured substrates for inverted perovskite solar cells. *Nature* **2023**, *624*, 289-294. http://dx.doi.org/10.1038/s41586-023-06745-7.
39. Mao, L., Yang, T., Zhang, H., Shi, J., Hu, Y., Zeng, P., Li, F., Gong, J., Fang, X., Sun, Y., Liu, X., Du, J., Han, A., Zhang, L., Liu, W., Meng, F., Cui, X., Liu, Z., Liu, M. Fully Textured, Production-Line Compatible Monolithic Perovskite/Silicon Tandem Solar Cells Approaching 29% Efficiency. *Adv. Mater.* **2022**, *34*, 2206193. http://dx.doi.org/10.1002/adma.202206193.
40. Phung, N., Verheijen, M., Todinova, A., Datta, K., Verhage, M., Al-Ashouri, A., Köbler, H., Li, X., Abate, A., Albrecht, S., Creatore, M. Enhanced Self-Assembled Monolayer Surface Coverage by ALD NiO in p-i-n Perovskite Solar Cells. *ACS Appl. Mater. Interfaces* **2021**, *14*, 2166-2176. http://dx.doi.org/10.1021/acsami.1c15860.
41. Yu, S., Xiong, Z., Zhou, H., Zhang, Q., Wang, Z., Ma, F., Qu, Z., Zhao, Y., Chu, X., Zhang, X., You, J. Homogenized NiOx nanoparticles for improved hole transport in inverted perovskite solar cells. *Sci* **2023**, *382*, 1399-1404. http://dx.doi.org/10.1126/science.adj8858.
42. Liu, T. L., Harake, M., Bent, S. F. Sequential Use of Orthogonal Self-Assembled Monolayers for Area-Selective Atomic Layer Deposition of Dielectric on Metal. *Adv. Mater. Interfaces*. **2022**, *10*, 2202134. http://dx.doi.org/10.1002/admi.202202134.
43. Clark, S. L., Montague, M., Hammond, P. T. Selective deposition in multilayer assembly: SAMs as molecular templates. *Supramol. Sci.* **1997**, *4*, 141-146. http://dx.doi.org/10.1016/s0968-5677(96)00055-7.
44. Chang, C.-W., Tseng, Y.-H., Hsu, C.-S., Chen, J.-T. Area-Selective Atomic Layer Deposition on Metal/Dielectric Patterns: Amphiphobic Coating, Vaporizable Inhibitors, and Regenerative Processing. *ACS Appl. Mater. Interfaces* **2023**, *15*, 28817-28824. http://dx.doi.org/10.1021/acsami.3c03752.
45. Farag, A., Feeney, T., Hossain, I. M., Schackmar, F., Fassl, P., Küster, K., Bäuerle, R., Ruiz-Preciado, M. A., Hentschel, M., Ritzer, D. B., Diercks, A., Li, Y., Nejand, B. A., Laufer, F., Singh, R., Starke, U., Paetzold, U. W. Evaporated Self-Assembled Monolayer Hole Transport Layers: Lossless Interfaces in p-i-n Perovskite Solar Cells. *Adv. Energy Mater.* **2023**, *13*, 2203982. http://dx.doi.org/10.1002/aenm.202203982.
46. Pujari, S. P., Scheres, L., Marcelis, A. T. M., Zuilhof, H. Covalent Surface Modification of Oxide Surfaces. *Angew. Chem. Int. Ed.* **2014**, *53*, 6322-6356. http://dx.doi.org/10.1002/anie.201306709.
47. Qiao, R., Zuo, L. Self-assembly monolayers boosting organic–inorganic halide perovskite solar cell performance. *J. Mater. Res.* **2018**, *33*, 387-400. http://dx.doi.org/10.1557/jmr.2017.477.
48. Kim, S. Y., Cho, S. J., Byeon, S. E., He, X., Yoon, H. J. Self-Assembled Monolayers as Interface Engineering Nanomaterials in Perovskite Solar Cells. *Adv. Energy Mater.* **2020**, *10*, 2002606. http://dx.doi.org/10.1002/aenm.202002606.
49. Zheng, X., Li, Z., Zhang, Y., Chen, M., Liu, T., Xiao, C., Gao, D., Patel, J. B., Kuciauskas, D., Magomedov, A., Scheidt, R. A., Wang, X., Harvey, S. P., Dai, Z., Zhang, C., Morales, D., Pruett, H., Wieliczka, B. M., Kirmani, A. R., Padture, N. P., Graham, K. R., Yan, Y., Nazeeruddin, M. K., McGehee, M. D., Zhu, Z., Luther, J. M. Co-deposition of hole-selective contact and absorber for improving the processability of perovskite solar cells. *Nat Energy* **2023**, *8*, 462-472. http://dx.doi.org/10.1038/s41560-023-01227-6.
50. Huang, Y., Yan, K., Wang, X., Li, B., Niu, B., Yan, M., Shen, Z., Zhou, K., Fang, Y., Yu, X., Chen, H., Zhang, L., Li, C. Z. High-Efficiency Inverted Perovskite Solar Cells via In Situ Passivation Directed Crystallization. *Adv. Mater.* **2024**, *36*, 2408101. http://dx.doi.org/10.1002/adma.202408101.
51. Jiang, W., Wang, D., Shang, W., Li, Y., Zeng, J., Zhu, P., Zhang, B., Mei, L., Chen, X. K., Xu, Z. X., Lin, F. R., Xu, B., Jen, A. K. Y. Spin-Coated and Vacuum-Processed Hole-Extracting Self-Assembled Multilayers with H-Aggregation for High-Performance Inverted Perovskite Solar Cells. *Angew. Chem. Int. Ed.* **2024**, *63*, e202411730. http://dx.doi.org/10.1002/anie.202411730.
52. Wang, G., Zheng, J., Duan, W., Yang, J., Mahmud, M. A., Lian, Q., Tang, S., Liao, C., Bing, J., Yi, J., Leung, T. L., Cui, X., Chen, H., Jiang, F., Huang, Y., Lambertz, A., Jankovec, M., Topič, M., Bremner, S., Zhang, Y.-Z., Cheng, C., Ding, K., Ho-Baillie, A. Molecular engineering of hole-selective layer for high band gap

perovskites for highly efficient and stable perovskite-silicon tandem solar cells. *Joule* **2023**, *7*, 2583-2594. http://dx.doi.org/10.1016/j.joule.2023.09.007.

53. Qu, G., Cai, S., Qiao, Y., Wang, D., Gong, S., Khan, D., Wang, Y., Jiang, K., Chen, Q., Zhang, L., Wang, Y.-G., Chen, X., Jen, A. K. Y., Xu, Z.-X. Conjugated linker-boosted self-assembled monolayer molecule for inverted perovskite solar cells. *Joule* **2024**, *8*, 2123-2134. http://dx.doi.org/10.1016/j.joule.2024.05.005.
54. He, X., Chen, H., Yang, J., Wang, T., Pu, X., Feng, G., Jia, S., Bai, Y., Zhou, Z., Cao, Q., Li, X. Enhancing Hole Transport Uniformity for Efficient Inverted Perovskite Solar Cells through Optimizing Buried Interface Contacts and Suppressing Interface Recombination. *Angew. Chem. Int. Ed.* **2024**, *63*, e202412601. http://dx.doi.org/10.1002/anie.202412601.
55. Ullah, A., Park, K. H., Nguyen, H. D., Siddique, Y., Shah, S. F. A., Tran, H., Park, S., Lee, S. I., Lee, K. K., Han, C. H., Kim, K., Ahn, S., Jeong, I., Park, Y. S., Hong, S. Novel Phenothiazine-Based Self-Assembled Monolayer as a Hole Selective Contact for Highly Efficient and Stable p-i-n Perovskite Solar Cells. *Adv. Energy Mater.* **2021**, *12*, 2103175. http://dx.doi.org/10.1002/aenm.202103175.
56. Liao, Q., Wang, Y., Hao, M., Li, B., Yang, K., Ji, X., Wang, Z., Wang, K., Chi, W., Guo, X., Huang, W. Green-Solvent-Processable Low-Cost Fluorinated Hole Contacts with Optimized Buried Interface for Highly Efficient Perovskite Solar Cells. *ACS Appl. Mater. Interfaces* **2022**, *14*, 43547-43557. http://dx.doi.org/10.1021/acsami.2c10758.
57. Kim, H. J., Han, G. S., Jung, H. S. Managing the lifecycle of perovskite solar cells: Addressing stability and environmental concerns from utilization to end-of-life. *eScience* **2024**, *4*, 100243. http://dx.doi.org/10.1016/j.esci.2024.100243.
58. Magomedov, A., Al-Ashouri, A., Kasparavičius, E., Strazdaite, S., Niaura, G., Jošt, M., Malinauskas, T., Albrecht, S., Getautis, V. Self-Assembled Hole Transporting Monolayer for Highly Efficient Perovskite Solar Cells. *Adv. Energy Mater.* **2018**, *8*, 1801892. http://dx.doi.org/10.1002/aenm.201801892.
59. Fu, Y. J., Li, Y., Xing, G. C., Cao, D. R. Surface passivation of perovskite with organic hole transport materials for highly efficient and stable perovskite solar cells. *Mater Today Adv* **2022**, *16*, 100300. http://dx.doi.org/10.1016/j.mtadv.2022.100300.
60. Li, Y., Zhang, L., Xia, J., Liu, T., Wang, K. Modifying PTAA/Perovskite Interface via 4-Butanediol Ammonium Bromide for Efficient and Stable Inverted Perovskite Solar Cells. *SMALL* **2023**, *19*, 2208243. http://dx.doi.org/10.1002/smll.202208243.
61. Wang, J., Bi, L., Huang, X., Feng, Q., Liu, M., Chen, M., An, Y., Jiang, W., Lin, F. R., Fu, Q., Jen, A. K. Y. Bilayer interface engineering through 2D/3D perovskite and surface dipole for inverted perovskite solar modules. *eScience* **2024**, *4*, 100308. http://dx.doi.org/10.1016/j.esci.2024.100308.
62. Wang, C., Jiang, Y., Xu, H., Zheng, N., Bai, G., Zha, Y., Qi, H., Bian, Z., Zhan, X., Liu, Z. Enhancing performance of tin-based perovskite solar cells via fused-ring electron acceptor. *eScience* **2023**, *3*, 100113. http://dx.doi.org/10.1016/j.esci.2023.100113.
63. Li, R., Liu, X., Chen, J. Opportunities and challenges of hole transport materials for high-performance inverted hybrid-perovskite solar cells. *Exploration* **2023**, *3*, 20220027. http://dx.doi.org/10.1002/exp.20220027.
64. Li, Y., Ji, L., Liu, R., Zhang, C., Mak, C. H., Zou, X., Shen, H.-H., Leu, S.-Y., Hsu, H.-Y. A review on morphology engineering for highly efficient and stable hybrid perovskite solar cells. *J. Mater. Chem. A* **2018**, *6*, 12842-12875. http://dx.doi.org/10.1039/c8ta04120b.
65. Sun, X., Zhu, Z., Li, Z. a. Recent advances in developing high-performance organic hole transporting materials for inverted perovskite solar cells. *Front. Optoelectron.* **2022**, *15*, 46. http://dx.doi.org/10.1007/s12200-022-00050-3.
66. Al-Ashouri, A., Magomedov, A., Roß, M., Jošt, M., Talaikis, M., Chistiakova, G., Bertram, T., Márquez, J. A., Köhnen, E., Kasparavičius, E., Levcenco, S., Gil-Escrig, L., Hages, C. J., Schlatmann, R., Rech, B., Malinauskas, T., Unold, T., Kaufmann, C. A., Korte, L., Niaura, G., Getautis, V., Albrecht, S. Conformal monolayer contacts with lossless interfaces for perovskite single junction and monolithic tandem solar cells. *Energy Environ. Sci.* **2019**, *12*, 3356-3369. http://dx.doi.org/10.1039/c9ee02268f.
67. Deng, X., Qi, F., Li, F., Wu, S., Lin, F. R., Zhang, Z., Guan, Z., Yang, Z., Lee, C. S., Jen, A. K. Y. Co-assembled Monolayers as Hole-Selective Contact for High-Performance Inverted Perovskite Solar Cells with

Optimized Recombination Loss and Long-Term Stability. *Angew. Chem. Int. Ed.* **2022**, *61*, e202203088. http://dx.doi.org/10.1002/anie.202203088.

68. Zhumagali, S., Li, C., Marcinskas, M., Dally, P., Liu, Y., Ugur, E., Petoukhoff, C. E., Ghadiyali, M., Prasetio, A., Marengo, M., Pininti, A. R., Azmi, R., Schwingenschlögl, U., Laquai, F., Getautis, V., Malinauskas, T., Aydin, E., Sargent, E. H., De Wolf, S. Efficient Narrow Bandgap Pb-Sn Perovskite Solar Cells Through Self-Assembled Hole Transport Layer with Ionic Head. *Adv. Energy Mater.* **2025**, 2404617. http://dx.doi.org/10.1002/aenm.202404617.
69. Liu, X., Ding, B., Han, M., Yang, Z., Chen, J., Shi, P., Xue, X., Ghadari, R., Zhang, X., Wang, R., Brooks, K., Tao, L., Kinge, S., Dai, S., Sheng, J., Dyson, P. J., Nazeeruddin, M. K., Ding, Y. Extending the π-Conjugated System in Spiro-Type Hole Transport Material Enhances the Efficiency and Stability of Perovskite Solar Modules. *Angew. Chem. Int. Ed.* **2023**, *62*, e202304350. http://dx.doi.org/10.1002/anie.202304350.
70. Wan, J., Zhang, Z., Lin, J., Li, Z., Liu, H., Li, Q., Yang, S., Wang, L. Simultaneously enhancing hole extraction and defect passivation with more conductive hole-selective self-assembled molecules for efficient inverted perovskite solar cells. *J. Mater. Chem. C* **2024**, *12*, 15644-15653. http://dx.doi.org/10.1039/d4tc02303j.
71. Wu, H., Wu, J., Zhang, Z., Guan, X., Wang, L., Deng, L.-l., Li, G., Abate, A., Li, M. Tailored Lattice-Matched Carbazole Self-Assembled Molecule for Efficient and Stable Perovskite Solar Cells. *J. Am. Chem. Soc.* **2025**, *147*, 8004-8011. http://dx.doi.org/10.1021/jacs.5c00629.
72. Dong, B., Wei, M., Li, Y., Yang, Y., Ma, W., Zhang, Y., Ran, Y., Cui, M., Su, Z., Fan, Q., Bi, Z., Edvinsson, T., Ding, Z., Ju, H., You, S., Zakeeruddin, S. M., Li, X., Hagfeldt, A., Grätzel, M., Liu, Y. Self-assembled bilayer for perovskite solar cells with improved tolerance against thermal stresses. *Nat Energy* **2025**, *10*, 342-353. http://dx.doi.org/10.1038/s41560-024-01689-2.
73. Li, Z., Tan, Q., Chen, G., Gao, H., Wang, J., Zhang, X., Xiu, J., Chen, W., He, Z. Simple and robust phenoxazine phosphonic acid molecules as self-assembled hole selective contacts for high-performance inverted perovskite solar cells. *Nanoscale* **2023**, *15*, 1676-1686. http://dx.doi.org/10.1039/d2nr05677a.
74. Tan, Q., Li, Z., Luo, G., Zhang, X., Che, B., Chen, G., Gao, H., He, D., Ma, G., Wang, J., Xiu, J., Yi, H., Chen, T., He, Z. Inverted perovskite solar cells using dimethylacridine-based dopants. *Nature* **2023**, *620*, 545-551. http://dx.doi.org/10.1038/s41586-023-06207-0.
75. Liu, M., Li, M., Li, Y., An, Y., Yao, Z., Fan, B., Qi, F., Liu, K., Yip, H. L., Lin, F. R., Jen, A. K. Y. Defect-Passivating and Stable Benzothiophene-Based Self-Assembled Monolayer for High-Performance Inverted Perovskite Solar Cells. *Adv. Energy Mater.* **2024**, *14*, 2303742. http://dx.doi.org/10.1002/aenm.202303742.
76. Jiang, W., Li, F., Li, M., Qi, F., Lin, F. R., Jen, A. K. Y. π-Expanded Carbazoles as Hole-Selective Self-Assembled Monolayers for High-Performance Perovskite Solar Cells. *Angew. Chem. Int. Ed.* **2022**, *61*, e202213560. http://dx.doi.org/10.1002/anie.202213560.
77. Wang, W., Liu, X., Wang, J., Chen, C., Yu, J., Zhao, D., Tang, W. Versatile Self-Assembled Molecule Enables High-Efficiency Wide-Bandgap Perovskite Solar Cells and Organic Solar Cells. *Adv. Energy Mater.* **2023**, *13*, 2300694. http://dx.doi.org/10.1002/aenm.202300694.
78. Yi, Z., Wang, W., He, R., Zhu, J., Jiao, W., Luo, Y., Xu, Y., Wang, Y., Zeng, Z., Wei, K., Zhang, J., Tsang, S.-W., Chen, C., Tang, W., Zhao, D. Achieving a high open-circuit voltage of 1.339 V in 1.77 eV wide-bandgap perovskite solar cells via self-assembled monolayers. *Energy Environ. Sci.* **2024**, *17*, 202-209. http://dx.doi.org/10.1039/d3ee02839a.
79. Jiang, W., Liu, M., Li, Y., Lin, F. R., Jen, A. K. Y. Rational molecular design of multifunctional self-assembled monolayers for efficient hole selection and buried interface passivation in inverted perovskite solar cells. *Chem. Sci.* **2024**, *15*, 2778-2785. http://dx.doi.org/10.1039/d3sc05485c.
80. Zhou, J., Luo, Y., Li, R., Tian, L., Zhao, K., Shen, J., Jin, D., Peng, Z., Yao, L., Zhang, L., Liu, Q., Zhang, S., Jin, L., Chu, S., Wang, S., Tian, Y., Xu, J., Zhang, X., Shi, P., Wang, X., Fan, W., Sun, X., Sun, J., Chen, L.-Z., Wu, G., Shi, W., Wang, H.-F., Deng, T., Wang, R., Yang, D., Xue, J. Molecular contacts with an orthogonal π-skeleton induce amorphization to enhance perovskite solar cell performance. *Nat. Chem.* **2025**, *17*, 564-570. http://dx.doi.org/10.1038/s41557-025-01732-z.
81. Li, C., Zhang, Z., Zhang, H., Yan, W., Li, Y., Liang, L., Yu, W., Yu, X., Wang, Y., Yang, Y., Nazeeruddin, M. K., Gao, P. Fully Aromatic Self-Assembled Hole-Selective Layer toward Efficient Inverted Wide-Bandgap

Perovskite Solar Cells with Ultraviolet Resistance. *Angew. Chem. Int. Ed.* **2023**, *63*, e202315281. http://dx.doi.org/10.1002/anie.202315281.

82. Guo, R., Zhang, X., Zheng, X., Li, L., Li, M., Zhao, Y., Zhang, S., Luo, L., You, S., Li, W., Gong, Z., Huang, R., Cui, Y., Rong, Y., Zeng, H., Li, X. Tailoring Multifunctional Self-Assembled Hole Transporting Molecules for Highly Efficient and Stable Inverted Perovskite Solar Cells. *Adv. Funct. Mater.* **2023**, *33*, 2211955. http://dx.doi.org/10.1002/adfm.202211955.
83. Truong, M. A., Funasaki, T., Ueberricke, L., Nojo, W., Murdey, R., Yamada, T., Hu, S., Akatsuka, A., Sekiguchi, N., Hira, S., Xie, L., Nakamura, T., Shioya, N., Kan, D., Tsuji, Y., Iikubo, S., Yoshida, H., Shimakawa, Y., Hasegawa, T., Kanemitsu, Y., Suzuki, T., Wakamiya, A. Tripodal Triazatruxene Derivative as a Face-On Oriented Hole-Collecting Monolayer for Efficient and Stable Inverted Perovskite Solar Cells. *J. Am. Chem. Soc.* **2023**, *145*, 7528-7539. http://dx.doi.org/10.1021/jacs.3c00805.
84. Wu, J., Yan, P., Yang, D., Guan, H., Yang, S., Cao, X., Liao, X., Ding, P., Sun, H., Ge, Z. Bisphosphonate-Anchored Self-Assembled Molecules with Larger Dipole Moments for Efficient Inverted Perovskite Solar Cells with Excellent Stability. *Adv. Mater.* **2024**, *36*, 2401537. http://dx.doi.org/10.1002/adma.202401537.
85. Su, T., Liu, W., Xu, H., Chen, H., Wong, K. L., Zhang, W., Su, Q., Wang, T., Xu, S., Liu, X., Lv, W., Geng, R., Yin, J., Song, X. Self-assembled hole-transport material incorporating biphosphonic acid for dual-defect passivation in NiOx-based perovskite solar cells. *J. Mater. Chem. A* **2024**, *12*, 33066-33075. http://dx.doi.org/10.1039/d4ta05776g.
86. Yalcin, E., Can, M., Rodriguez-Seco, C., Aktas, E., Pudi, R., Cambarau, W., Demic, S., Palomares, E. Semiconductor self-assembled monolayers as selective contacts for efficient PiN perovskite solar cells. *Energy Environ. Sci.* **2019**, *12*, 230-237. http://dx.doi.org/10.1039/c8ee01831f.
87. Aktas, E., Pudi, R., Phung, N., Wenisch, R., Gregori, L., Meggiolaro, D., Flatken, M. A., De Angelis, F., Lauermann, I., Abate, A., Palomares, E. Role of Terminal Group Position in Triphenylamine-Based Self-Assembled Hole-Selective Molecules in Perovskite Solar Cells. *ACS Appl. Mater. Interfaces* **2022**, *14*, 17461-17469. http://dx.doi.org/10.1021/acsami.2c01981.
88. Yalcin, E., Aktas, E., Mendéz, M., Arkan, E., Sánchez, J. G., Martínez-Ferrero, E., Silvestri, F., Barrena, E., Can, M., Demic, S., Palomares, E. Monodentate versus Bidentate Anchoring Groups in Self-Assembling Molecules (SAMs) for Robust p–i–n Perovskite Solar Cells. *ACS Appl. Mater. Interfaces* **2023**. http://dx.doi.org/10.1021/acsami.3c13727.
89. Zhu, J., Luo, Y., He, R., Chen, C., Wang, Y., Luo, J., Yi, Z., Thiesbrummel, J., Wang, C., Lang, F., Lai, H., Xu, Y., Wang, J., Zhang, Z., Liang, W., Cui, G., Ren, S., Hao, X., Huang, H., Wang, Y., Yao, F., Lin, Q., Wu, L., Zhang, J., Stolterfoht, M., Fu, F., Zhao, D. A donor–acceptor-type hole-selective contact reducing non-radiative recombination losses in both subcells towards efficient all-perovskite tandems. *Nat Energy* **2023**, *8*, 714-724. http://dx.doi.org/10.1038/s41560-023-01274-z.
90. Zhou, Y., Huang, X., Zhang, J., Zhang, L., Wu, H., Zhou, Y., Wang, Y., Wang, Y., Fu, W., Chen, H. Interfacial Modification of NiOx for Highly Efficient and Stable Inverted Perovskite Solar Cells. *Adv. Energy Mater.* **2024**, *14*, 2400616. http://dx.doi.org/10.1002/aenm.202400616.
91. Sun, X., Fan, H., Xu, X., Li, G., Gu, X., Luo, D., Shan, C., Yang, Q., Dong, S., Miao, C., Xie, Z., Lu, G., Wang, D. H., Sun, P. P., Kyaw, A. K. K. A Fluorination Strategy and Low-Acidity Anchoring Group in Self-Assembled Molecules for Efficient and Stable Inverted Perovskite Solar Cells. *Chem. Eur. J.* **2024**, *30*, e202400629. http://dx.doi.org/10.1002/chem.202400629.
92. Truong, M. A., Funasaki, T., Adachi, Y., Hira, S., Tan, T., Akatsuka, A., Yamada, T., Iwasaki, Y., Matsushige, Y., Kaneko, R., Asahara, C., Nakamura, T., Murdey, R., Yoshida, H., Kanemitsu, Y., Wakamiya, A. Molecular Design of Hole-Collecting Materials for Co-Deposition Processed Perovskite Solar Cells: A Tripodal Triazatruxene Derivative with Carboxylic Acid Groups. *J. Am. Chem. Soc.* **2025**, *147*, 2797-2808. http://dx.doi.org/10.1021/jacs.4c15857.
93. Zhang, Z., Zhu, R., Tang, Y., Su, Z., Hu, S., Zhang, X., Zhang, J., Zhao, J., Xue, Y., Gao, X., Li, G., Pascual, J., Abate, A., Li, M. Anchoring Charge Selective Self-Assembled Monolayers for Tin–Lead Perovskite Solar Cells. *Adv. Mater.* **2024**, *36*, 2312264. http://dx.doi.org/10.1002/adma.202312264.
94. Zhao, K., Yao, L., Liu, C., Yavuz, I., Shen, J., Shi, P., Zhang, X., Luo, Y., Jin, D., Tian, Y., Wang, S., Fan, W., Xu, J., Liu, Q., Wang, X., Tian, L., Liu, R., Değer, C., Wang, R., Xue, J. Tailoring the π-conjugation in self-

assembled hole-selective molecules for perovskite photovoltaics. *Sci. China Mater*. **2024**. http://dx.doi.org/10.1007/s40843-024-3093-9.

95. Wang, Y., Liao, Q., Chen, J., Huang, W., Zhuang, X., Tang, Y., Li, B., Yao, X., Feng, X., Zhang, X., Su, M., He, Z., Marks, T. J., Facchetti, A., Guo, X. Teaching an Old Anchoring Group New Tricks: Enabling Low-Cost, Eco-Friendly Hole-Transporting Materials for Efficient and Stable Perovskite Solar Cells. *J. Am. Chem. Soc.* **2020**, *142*, 16632-16643. http://dx.doi.org/10.1021/jacs.0c06373.
96. Zhang, S., Wu, R., Mu, C., Wang, Y., Han, L., Wu, Y., Zhu, W.-H. Conjugated Self-Assembled Monolayer as Stable Hole-Selective Contact for Inverted Perovskite Solar Cells. *ACS Materials Lett*. **2022**, *4*, 1976-1983. http://dx.doi.org/10.1021/acsmaterialslett.2c00799.
97. Afraj, S. N., Kuan, C. H., Cheng, H. L., Wang, Y. X., Liu, C. L., Shih, Y. S., Lin, J. M., Tsai, Y. W., Chen, M. C., Diau, E. W. G. Triphenylamine-Based Y-Shaped Self-Assembled Monolayers for Efficient Tin Perovskite Solar Cells. *SMALL* **2024**, *21*, 2408638. http://dx.doi.org/10.1002/smll.202408638.
98. Cheng, H., Huang, Z.-S. Self-assembled organic molecules with a fused aromatic ring as hole-transport layers for inverted perovskite solar cells: the effect of linkers on performance. *New J. Chem.* **2024**, *48*, 6833-6841. http://dx.doi.org/10.1039/d4nj00154k.
99. Guo, H., Liu, C., Hu, H., Zhang, S., Ji, X., Cao, X.-M., Ning, Z., Zhu, W.-H., Tian, H., Wu, Y. Neglected acidity pitfall: boric acid-anchoring hole-selective contact for perovskite solar cells. *Natl. Sci. Rev.* **2023**, *10*, nwad057. http://dx.doi.org/10.1093/nsr/nwad057.
100. Guo, S., Yang, X., Zhang, Q., Jin, X., Zhang, D., Guo, Y., Zhou, H., Huang, J., Su, J., Xu, B. Fused Carbazole-based Self-Assembled Monolayers Enable Efficient Perovskite Solar Cells and Perovskite Light-Emitting Diodes. *Adv. Opt. Mater.* **2024**, *12*, 2401617. http://dx.doi.org/10.1002/adom.202401617.